Sex, stress and UCP2:
mitochondria illuminate microglial identity beyond the dichotomy

Authors

Margaret E Maes[1], Gloria Colombo[1], Felix Sternberg [2], Elena E Pohl[2], Sandra Siegert[1†]

Affiliations

[1] Institute of Science and Technology Austria (ISTA), Am Campus 1, 3400 Klosterneuburg, Austria

[2] Institute of Physiology, Pathophysiology and Biophysics, University of Veterinary Medicine, Veterinärplatz 1, 1210 Vienna, Austria

† Corresponding author: ssiegert@ist.ac.at

Abstract

Environmental cues influence microglial interaction with their neuronal landscape, often causing changes in microglial functional identity. This process demands rapid energy production, which is supported by an optimized mitochondrial network. Whether mitochondrial adaptations define a microglial functional state is unknown due to limitations in mitochondrial visualization and manipulation within their microenvironment.

Here, we investigate the mitochondrial network of individual microglia in physiological and dysfunctional conditions during a naïve or injury-induced mouse retinal environment. After optic nerve crush (ONC) injury, we identify mitochondrial and microglial phenotypic remodeling that is distinct from the naïve environment. Remarkably, knockout of uncoupling protein 2 (UCP2) causes transient, stress-induced mitochondrial hyperfusion only in males after ONC, even though both sexes suffer from increased intrinsic stress levels. When we compare key metabolic genes between sexes in physiological conditions, only males exhibit a metabolic transition towards glycolysis in the injury-induced environment, which attenuates in UCP2 knockout resulting in acutely accelerated retinal ganglion cell death. Our data shows that the cell-extrinsic ONC environment and cell-intrinsic UCP2^{KO} manipulation triggers several microglial states distinguishable by mitochondrial networks that are heavily influenced by sex and injury-induced stress.

Key words

Microglia, mitochondria, UCP2, retina, sex, stress, hyperfusion, optic nerve crush

Introduction

Microglia transiently and dynamically respond to a myriad of cues within their microenvironment, ranging from local surveillance to active engagement in removing cellular components (Hanisch and Kettenmann, 2007; Salter and Stevens, 2017). An unresolved challenge is how to define this spectrum of microglial functional states (Paolicelli et al., 2022), which has been described by single cell transcriptomes and morphological analyses (Colombo et al., 2021; Masuda et al., 2020; Stogsdill et al., 2022). Moreover, systemic factors such as sex, age, and genetic background influence the microglial functional state. Whereas -omics studies are often limited in their readout to a sole factor *e.g.,* gene transcripts, a multifaceted readout for microglia within their microenvironment would be desirable.

A cell's energetic demands predominantly rely on mitochondrial function, where ATP production is optimized through the dynamic processes of organelle fission and fusion (Mishra and Chan, 2016; Rambold and Pearce, 2018). In physiological conditions, these mitochondrial dynamics allow for exchange of matrix content or elimination of dysfunctional organelles, creating a balanced, homeostatic mitochondrial network (Youle and van der Bliek, 2012). Under high energy demand, this equilibrium is disrupted, resulting in a more fragmented mitochondrial network as the cell shifts from oxidative phosphorylation (OXPHOS) to favor glycolysis (Buck et al., 2016). In contrast, mitochondria can also take on a hyperfused morphology, which is reflected by a filamentous, highly connected mitochondrial network (Gomes et al., 2011; Tondera et al., 2009). This hyperfused network serves as a short-term cell survival mechanism to increase membrane potential and calcium accumulation enhancing ATP levels in stressed environments (Das and Chakrabarti, 2020; Gomes et al., 2011; Mitra et al., 2009; Tondera et al., 2009; Wai and Langer, 2016). Therefore, mitochondrial network connectivity is a critical parameter to discriminate the intrinsic cellular energetic demands.

Transcriptomic studies frequently identify differentially expressed metabolism-associated genes in microglia during development and disease progression (Baik et al., 2019; Bernier et al., 2020; He et al., 2022; Ulland et al., 2017), that is paralleled in macrophages outside the CNS (Borst et al., 2019; Jha et al., 2015). One such gene is uncoupling protein 2 (UCP2, Slc25a8) which is found in immune cells (Arsenijevic et al., 2000; Pecqueur et al., 2001; Rupprecht et al., 2012), including microglia (Siegert et al., 2012), as well as in cells that

favor glycolysis such as, rapidly proliferating cells or stem cells (Horimoto et al., 2004; Rupprecht et al., 2014, 2019; Zhang et al., 2011). The two main transport functions of UCP2 are the fatty acids-induced import of protons to bypass ATP synthetase (Ježek et al., 2018) and export of Krebs cycle metabolites to limit the oxidation of acetyl-CoA producing substrates (Vozza et al., 2014). Loss of UCP2 has recently been reported to inhibit mitochondrial dynamics, ATP production, and microglial inflammation in the hypothalamus after high fat diet (Kim et al., 2019; Toda et al., 2016). This makes UCP2 a promising candidate to manipulate mitochondria and determine their impact on the microglial functional state.

One major limitation in assessing mitochondrial networks *in vivo* is targeting cell type-specific mitochondria, which can easily be achieved *in vitro*. However, studying microglial properties *in vitro* or *ex vivo* leads to significant morphological and transcriptomic alterations that do not recapitulate the *in vivo* environment (Galatro et al., 2017; Gosselin et al., 2017; Hammond et al., 2019; Matcovitch-Natan et al., 2016). Moreover, sex hormones have been shown to influence microglial function (Villa et al., 2018), further emphasizing the need to investigate microglia within their microenvironment. Thus, we must address the following two challenges: first, their selective visualization and second, their targeted manipulation with minimal external interference.

Here, we generated a mouse model that labels mitochondria exclusively within microglia, allowing us to perform multifaceted analysis on single microglia in their microenvironment. We focused on the retina where microglial populations are distinctly separated in the outer- and inner plexiform layers (OPL and IPL, respectively). Then, we selectively knocked out UCP2 to establish a dysfunctional mitochondrial condition. Finally, we performed optic nerve crush (ONC), which damages the axonal projections of retinal ganglion cells (RGCs) in the optic nerve but leaves the dura and the blood vessels intact (Williams et al., 2020). As a consequence, microglia in the inner plexiform layer (IPL) respond to RGCs undergoing apoptosis within the first week (Liu et al., 2012; Mac Nair et al., 2016; Wohl et al., 2010). Remarkably, our multifaceted mitochondria and microglial analysis *in vivo* revealed sexual-dimorphic microglia functional states based on the ONC and the loss of UCP2. This underscores the necessity of evaluating sex in microglia in neuropathological environments.

102 **Results**

103

104 **Resolving mitochondrial networks of microglia in naïve environments**

105 To selectively visualize mitochondria in microglia, we took advantage of the mouse reporter
106 line PhAM$^{fl/fl}$, which labels mitochondria with a Dendra2-tag (Pham et al., 2012). We crossed
107 this mouse with the *Cx3cr1*^{CreERT2} mouse model (Yona et al., 2013) (**Figure 1A**). Upon
108 tamoxifen induction, only microglia detected with IBA1 (ionized calcium binding adaptor
109 molecule 1) expressed the Dendra2-tag in the retina (**Figure 1B-C**). Throughout this study,
110 we will refer to this tamoxifen-induced mouse model *Cx3cr1*$^{CreERT2/+}$/PhAM$^{fl/fl}$ as μG^{mito}
111 mice. To perform targeted mitochondrial manipulation, we revisited our retinal transcriptome
112 dataset for mitochondria-associated genes and confirmed high expression of uncoupling
113 protein 2 (UCP2) in retinal microglia (**Figure S1A-B**) (Siegert et al., 2012). Since recent
114 single cell RNA-sequencing studies also supported UCP2 transcript enrichment in retinal
115 microglia (Hoang et al., 2020; O'Koren et al., 2019), we generated a tamoxifen-inducible
116 microglia-specific UCP2-knockout mouse model by crossing the *Ucp2*$^{fl/fl}$ mouse (Kong et al.,
117 2010) with μG^{mito} (**Figure 1D**). This *Cx3cr1*$^{CreERT2/+}$/Pham$^{fl/fl}$/*Ucp2*$^{fl/fl}$ mouse model,
118 hereafter referred to μG^{mito}UCP2^{KO}, also showed microglia-selective mitochondrial labeling
119 (**Figure 1E-F**). To verify UCP2 depletion, we isolated retinal microglia with fluorescence-
120 activated cell sorting (FACS) using their Dendra2-tag (**Figure S1C**). We found that the *Ucp2*
121 transcript was undetectable three weeks after tamoxifen induction (**Figure S1D**). Similarly,
122 UCP2 protein expression decreased after 4-OHT (4-hydroxytamoxifen) exposure in murine
123 primary microglia culture (**Figure S1E-G**).

124 After establishing both mouse models, we profiled the mitochondrial network of microglia at
125 single-cell resolution (**Figure 1C**, **F**). We first observed that the mitochondria of both
126 conditions intersect at the soma and extend through the primary microglial processes. To
127 further evaluate these networks, we assessed three parameters: mitochondrial connectivity
128 based on the median organelle volume and total number of organelles per cell (**Figure 1G**),
129 the percentage of mitochondria in microglia as an estimation of mitochondrial biogenesis
130 (Ron-Harel et al., 2016) (**Figure 1H**), and perinuclear mitochondrial localization to gain
131 insights into transcriptional activity (Al-Mehdi et al., 2012) (**Figure 1I**). All mitochondrial
132 parameters were indistinguishable between μG^{mito} and μG^{mito}UCP2^{KO} microglia in the
133 homeostatic environment (**Figure 1G-I**). Thus, we established the balanced mitochondrial
134 networks of microglia within their homeostatic microenvironment, which are not critically
135 dependent on UCP2 in physiological conditions.

136

137 **Optic nerve crush upregulates microglial UCP2 and alters the mitochondrial network**

138 Next, we were interested to trigger an injury-induced environment in the retina. For this, we
139 took advantage of the optic nerve crush (ONC) model (Levkovitch-Verbin et al., 2000),
140 where the retinal ganglion cell (RGC) axons posterior to the optic disc are mechanically
141 injured (**Figure 2A**). This induces RGC apoptosis (**Figure S2A**) and microglial reactivity
142 (**Figure 2B**) (Li et al., 1999; Wohl et al., 2010). To determine the time of robust microglial
143 response after ONC, we collected retinas 1, 5, and 14 days after either ONC or sham injury
144 and compared their morphological changes using Sholl analysis (**Figure S2B-C**). The most
145 pronounced adaptation occurred at 5 days after ONC, whereas the sham surgery-induced
146 response was no longer visible (**Figure S2C**). In the injury-induced environment, microglia
147 upregulate the endosomal-lysosomal marker CD68 (Bauer et al., 1994; Damoiseaux et al.,
148 1994). Thus, we assessed the percentage volume of CD68 per microglia volume and
149 confirmed the Sholl analysis identified response pattern at 5 days (**Figure S2D-E**). Microglia
150 in the outer plexiform layer (OPL) reflected transient morphological adaptation at 5 days but
151 without changes in CD68 volume (**Figure S2F-I**). When we analyzed the *Ucp2* transcript
152 level in μG^{mito} microglia from untreated (naïve) mice or mice 5 days after ONC, the *Ucp2*
153 transcript was significantly upregulated (**Figure 2C**) indicating *Ucp2* involvement in the
154 ONC microglial response at 5 days after injury.

155 Next, we performed the single microglia analysis and compared microglial morphology,
156 CD68, and the mitochondrial network in naïve (**Figure 2D-F**) and 5 days after ONC in μG^{mito}
157 mice (**Figure 2G-I**). Microglia reduced their branching complexity shown by an increased
158 number of Sholl intersections closer to the soma (**Figure 2J**). Furthermore, they expressed a
159 greater percentage volume of CD68, with increased CD68-vesicle localization in the
160 peripheral microglial processes (**Figure 2K-L**). When we looked at the mitochondrial profile,
161 the median mitochondrial volume was reduced while the total number of organelles increased
162 (**Figure 2M**). This indicates a more fragmented mitochondrial network and suggests changes
163 in metabolic demand (Buck et al., 2016). We also found mitochondrial content (**Figure 2N**)
164 and localization to the perinuclear region (**Figure 2O**) significantly increased. This data
165 shows that microglia upregulate UCP2 and adapt their mitochondrial network in the injury-
166 induced microenvironment.

167

168 **Loss of UCP2 elicits a sexually dimorphic microglial response after ONC**
169 Previous studies in the arcuate nucleus of the hypothalamus suggested that loss of UCP2
170 affects microglial reactivity and prevented mitochondrial alterations after high fat-diet (Kim
171 et al., 2019). Surprisingly, when we performed ONC in the $UCP2^{KO}$ condition (**Figure 3**),
172 mitochondria were more fragmented (**Figure 3H-J**), showed an overall increased volume per
173 microglia (**Figure 3K**), and localized to the perinuclear space (**Figure 3L**). This is in line
174 with microglial adaptations that we observed in **Figure 2**, which recapitulated the reduced
175 microglia branching complexity (**Figure 3A-C**), and increased CD68 volume (**Figure 3D-G**).
176
177 To resolve this and obtain unbiased insights into the relationship between the parameters, we
178 applied principal component analysis (PCA) across experimental groups (μG^{mito}_{naive}, μG^{mito}-
179 $_{ONC}$, $\mu G^{mito}UCP2^{KO}_{naive}$, $\mu G^{mito}UCP2^{KO}_{ONC}$, see Methods for parameter descriptions). In the
180 principal component (PC) space, each dot represents a microglia profile, which contains all
181 parameters for a single-cell within a defined condition and environment. In the homeostatic
182 environment, the profiles of naïve μG^{mito} and $\mu G^{mito}UCP2^{KO}$ intermingled within the same
183 PC space (**Figure 4A**), indicating that UCP2 loss does not affect the microglial profile at
184 baseline conditions as indicated in **Figure 1G-I**. Also, we did not find any polarization in the
185 naïve clusters analyzed at homeostatic conditions that would point to sexual differences of
186 the microglial profiles (**Figure 4B-C**).
187 In the ONC-induced environment, individual microglial profiles transitioned away from their
188 naïve counterparts along the first PC (PC1, **Figure 4D**). Here, we observed a difference
189 between μG^{mito} and $\mu G^{mito}UCP2^{KO}$ conditions, in which the microglia profiles from the
190 $UCP2^{KO}$ were positioned between μG^{mito}_{naive} and μG^{mito}_{ONC} profiles. Moreover, they showed
191 an increased spread along the second PC (PC2) indicating that $UCP2^{KO}$ alters the microglia
192 profile. Strikingly, sex explained the segregation of $\mu G^{mito}UCP2^{KO}_{ONC}$ along PC2. While
193 μG^{mito}_{ONC} ♂ and ♀ profiles remained indistinguishable (**Figure 4E**), there was distinct
194 separation between ♂ and ♀ microglia in $\mu G^{mito}UCP2^{KO}_{ONC}$ (**Figure 4F**). Contrary to
195 previous reports, our data suggests that UCP2 loss causes a sex-specific microglial profile
196 after ONC injury.
197
198 **Male $UCP2^{KO}$ microglia exhibit hyperfused mitochondria after ONC**
199 To identify which of the analyzed parameters in the microglia profile strongly contributed to
200 the sex-specific differences of $\mu G^{mito}UCP2^{KO}_{ONC}$ (**Figure 4F**), we looked at the PC loadings.

201 The top contributing parameters in PC1 were the Sholl index and CD68, whereas in PC2 they
202 were mitochondria-derived (**Figure S3A**). To determine whether the sex-dependency
203 persisted with a subset of parameters, we repeated the PCA separately on the mitochondrial
204 (**Figure 5A-C**), or the Sholl index and CD68 parameters (**Figure S3B-D**). The Sholl index
205 and CD68 volume PCA showed no evidence of sex-dependency (**Figure S3C-D**). In contrast,
206 the mitochondrial parameters recapitulated the segregation (**Figure 5C**) as illustrated for
207 naïve and ONC counterparts (**Figure 4D**). The microglial profiles from the μG^{mito} spread
208 along PC1 and importantly, the sex-specific segregation of $\mu G^{mito}UCP2^{KO}{}_{ONC}$ persisted along
209 PC2 (**Figure 5C**). The median mitochondrial volume and the number of mitochondria were
210 the influential factors for PC1 (**Figure S3E**). These parameters suggested a more fragmented
211 mitochondrial network in ♂ and ♀$\mu G^{mito}{}_{ONC}$ microglia (**Figure S3F-G**) – an anticipated
212 mitochondrial network change after injury. Interestingly, ♀$\mu G^{mito}UCP2^{KO}{}_{ONC}$ behaved
213 similar to $\mu G^{mito}{}_{ONC}$ microglia and intermingled with their profiles (**Figure 5A-C**). In
214 contrast, ♂$\mu G^{mito}UCP2^{KO}{}_{ONC}$ lacked this fragmentation (**Figure S3F-G**) and instead
215 significantly increased the percentage of mitochondrial volume per microglia (**Figure S3G**).
216 This parameter also explained the variance along PC2 (**Figure S3E**). Together, these three
217 parameters suggested a hyperfused mitochondria network (**Figure S3F-H**). Therefore, we
218 closely re-examined the mitochondria within the microglia and found the mitochondrial
219 network was highly connected in ♂$\mu G^{mito}UCP2^{KO}{}_{ONC}$ microglia (**Figure 5D-E**). When we
220 plotted the volume of each organelle within a cell, rather than the median mitochondrial
221 volume, we found that ♂$\mu G^{mito}UCP2^{KO}{}_{ONC}$ microglia had significantly more organelles with
222 large volumes (> $20\mu m^3$) compared to females (**Figure 5D-E**). These data illustrate that
223 UCP2 loss induced a hyperfused mitochondrial network in male microglia after ONC.
224
225 **Sexually dimorphic metabolic stress response elucidates mitochondrial hyperfusion**
226 Mitochondrial hyperfusion has been described *in vitro* as a transient phenotype that protects
227 cellular and mitochondrial health in stress-induced environments (Gomes et al., 2011;
228 Tondera et al., 2009). To assess whether the hyperfused mitochondrial network is transient,
229 we included individual microglia analyzed at day 14 after ONC in the mitochondrial PCA
230 analysis. At 14 days, all microglial profiles formed a single cluster in the PC space (**Figure**
231 **6A**, **S4A**) including the ♂$\mu G^{mito}UCP2^{KO}{}_{ONC}$. Accordingly, the number of large-volume
232 mitochondria was reduced (**Figure 6B**), suggesting that the hyperfused phenotype at day 5 is
233 transient after injury, reflecting a unique microglial profile.

234 Since the hyperfused mitochondrial network is an adaptive mechanism to manage cellular
235 stress (Tondera et al., 2009), we interrogated the relative transcript expression of key
236 regulators of metabolic pathways and cellular stress response (**Figure 6C**): *Pgc1-a*
237 (proliferator-activated receptor gamma coactivator 1- alpha) and *Nrf1* (nuclear respiratory
238 factor 1) for oxidative phosphorylation (OXPHOS); *Hif1-a* (hypoxia inducible factor 1 alpha)
239 for glycolytic regulation (Finck and Kelly, 2006); the oxidative stress indicator *Sod1*
240 (superoxide dismutase 1); and *Cd68* (cluster of differentiation 68) as microglial cell stress
241 markers (Bauer et al., 1994; Spanier et al., 2009). After RT-qPCR of FACSorted microglia,
242 we performed PCA to identify whether conditions separate in the PC space and which
243 variables contribute to this segregation. The PC loadings indicated that metabolic genes
244 *Pgc1-a* and *Nrf1* strongly influenced PC1, whereas the stress genes affected PC2 (**Figure**
245 **S4B**). In the naïve environment, the sex of both conditions shared the same PC space (**Figure**
246 **S4C**). As expected, UCP2^{KO} condition separated from μG^{mito} along PC2 for both sexes
247 (**Figure 6D**), suggesting a more stressed environment already in the naïve environment.
248 Surprisingly, upon ONC we observed a prominent difference between male and female
249 microglia in both μG^{mito} and μG^{mito}UCP2^{KO}. Whereas ♀μG$^{mito}_{ONC}$ microglia occupied the
250 same PC space as in naïve condition, ♂μG$^{mito}_{ONC}$ microglia moved along the metabolism-
251 associated PC1 (**Figure 6E**). When we referenced the individual genes, ♂μG$^{mito}_{ONC}$
252 microglia significantly shifted towards a more glycolytic metabolism with decreased *Pgc1-α*
253 and *Nrf1* and some change in *Hif1-α* transcript level (**Figure S4D**). In contrast, ♀μG$^{mito}_{ONC}$
254 microglia transcript levels were unaffected (**Figure S4E**). Upon UCP2^{KO} in the injury-
255 induced environment, this metabolic shift was less pronounced in males compared to
256 ♂μG$^{mito}_{ONC}$ (**Figure 6F**) suggesting that male microglia response was attenuated. In fact,
257 ♂μG^{mito}UCP2$^{KO}_{ONC}$ had greater *Sod1* upregulation than ♀μG^{mito}UCP2$^{KO}_{ONC}$ or either sex in
258 μG^{mito} conditions (**Figure S4F**).
259
260 Finally, to obtain insights whether increased metabolic stress in ♂μG^{mito}UCP2$^{KO}_{ONC}$
261 microglia impacts retinal ganglion cell (RGC) survival after injury, we assessed RGC
262 numbers using the marker RBPMS (RNA binding protein with multiple splicing) (Rodriguez
263 et al., 2014). ♂μG^{mito}UCP2$^{KO}_{ONC}$ had significantly more RGC loss at day 5 after ONC
264 compared to females (**Figure 6G**). However, this difference was transient as the loss of
265 RGCs was similar between sexes by day 14 (**Figure 6G**).

266 Overall, this data indicates that the hyperfused mitochondrial network in ♂$\mu G^{mito}UCP2^{KO}{}_{ONC}$
267 is due to greater intrinsic stress of ♂microglia, resulting in an acute adverse effect in the
268 microenvironment.
269
270 **Discussion**
271 Extensive *in vitro* studies have shown that cellular energy demands of immune cells critically
272 depend on an optimized equilibrium of mitochondrial fission and fusion (Rambold and
273 Pearce, 2018). Whether this holds true for microglia *in vivo* is unknown due to the technical
274 limitations of selective mitochondrial visualization and manipulation, two difficulties that we
275 overcome here. We demonstrate that distinct mitochondrial networks reflect *in vivo* microglia
276 functional states dependent on the mitochondrial condition (μG^{mito} or $\mu G^{mito}UCP2^{KO}$) and the
277 local environment (naïve or ONC).
278
279 In the naïve environment, mitochondria exhibit a balanced network with organelles spanning
280 the primary microglial processes (**Figure 1C**, **F-I**). However, after ONC injury, mitochondria
281 of μG^{mito} accumulated in the perinuclear region (**Figure 2I**, **O**), increased their content
282 (**Figure 2N**) and became more fragmented throughout the microglial processes and soma
283 (**Figure 2M**). This corroborates reports of mitochondrial fragmentation after
284 lipopolysaccharide stimulation of microglia *in vitro* and of increased mitochondrial mass in
285 immature microglia of germ-free environment *ex vivo* (Erny et al., 2021; Nair et al., 2019;
286 Park et al., 2013). We also found unexpected mitochondrial alterations in the $\mu G^{mito}UCP2^{KO}$
287 condition (**Figure 3I**, **J-L**) (Toda et al., 2016), which we further elucidated using an unbiased
288 PCA approach (**Figure 4**). PCA indicated that the mitochondrial parameters explained the
289 sex-dependent variance among the ONC-induced $\mu G^{mito}UCP2^{KO}$ microglia profiles.
290 Remarkably, this sex-specific difference persisted even if we performed the PCA for the
291 mitochondrial parameters alone (**Figure 5C**) and pointed towards the hyperfused
292 mitochondrial network present exclusively in males (**Figure 5D**). Overall, our analysis
293 supports that mitochondrial networks elucidate microglial functional states in their well-
294 defined microenvironments with sex as a confounding factor.
295
296 Mitochondrial hyperfusion has predominantly been described in mouse embryonic fibroblast
297 cell lines (Gomes et al., 2011; Tondera et al., 2009). Here we report that this phenotype also
298 occurs *in vivo*. Until now, UCP2 has been implicated in cell metabolism (Rupprecht et al.,
299 2019) and stress responses (Smorodchenko et al., 2017) even though its function is not fully

resolved (Arsenijevic et al., 2000; Faas et al., 2021; Vozza et al., 2014). Our data shows that microglia lacking UCP2 have increased intrinsic stress in the naïve environment (**Figure S4F**), aligning with previous literature (Kim et al., 2019; Yasumoto et al., 2021). However, the added extrinsic stressor of the injury-induced environment provoked a hyperfused mitochondrial network, a hallmark of a pro-survival mechanism to manage extensive intracellular stress (Wai and Langer, 2016). Interestingly, recent studies reported that $UCP2^{KO}$ in microglia prevents mitochondrial fission (Kim et al., 2019; Toda et al., 2016), which could be one interpretation of our results. However, with a whole-cell representation of the mitochondrial network, combined with the contrasting sex-dependent phenotypes, we can conclude that UCP2 does not directly mediate fission, but rather affects stress-induced mitochondrial network dynamics.

The hyperfused mitochondrial phenotype in male $UCP2^{KO}$ was striking, but transient, therefore we cannot exclude that females exhibit a similar phenotype at different injury time points. However, we already observed a differing metabolic gene response after ONC in the physiological mitochondria condition (**Figure 6**), emphasizing an impact of sex prior to additional stressors. Sex hormones have been suggested to drive microglial dimorphisms by epigenetically shaping microglia during development and continuing to influence them during adulthood (Baker et al., 2004; Thion et al., 2018; Villa et al., 2018; Yang et al., 2004). For example, estrogens are implicated to be protective under higher cell-stress conditions (Colombo et al., 2021; Man et al., 2003; Nakazawa et al., 2006; Nuzzi and Caselgrandi, 2022; Quigley and Broman, 2006). Whereas in $UCP2^{KO}$, both sexes showed increased intrinsic stress response in the naïve environment (**Figure 6D**), only the males exhibited acute acceleration of RGC death 5 days after ONC (**Figure 6G-H**), a time point of robust microglia response and peak RGC apoptotic commitment (Galindo-Romero et al., 2013; Maes et al., 2017). Such sex-specific susceptibility has only been reported in long-term RGC degenerative models (Libby et al., 2005). Our data suggests that microglia play an early protective role after ONC, even if short-lived, which is contrary to previous reports (Hilla et al., 2017).

In summary, we demonstrate that mitochondrial networks provide another modality to interrogate the microglial functional state and highlights the importance of sex. This will have substantial implications as we begin to address immunometabolism-related targets for therapy in neurodegenerative diseases.

334 **Author contributions**

335 M.M. and S.S. conceived, developed experimental design and analysis, and wrote the
336 manuscript. M.M., F.S. and E.E.P. conceived and verified UCP2 protein knockout. M.M.
337 performed experiments, data and statistical analysis, and created figures. G.C. performed
338 FACS, RT-qPCR experiments, and data analysis. All authors provided comment and
339 discussion on the manuscript and approved the final version.

340

341 **Acknowledgements**

342 We thank the Scientific Service Units (SSU) of ISTA through resources provided by the
343 Imaging and Optics Facility (IOF), the Lab Support Facility (LSF), and the Pre-Clinical
344 Facility (PCF) team, specifically Sonja Haslinger and Michael Schunn for excellent mouse
345 colony management and support. This research was partly supported by the FWF
346 Sonderforschungsbereich F83 (to E.E.P). We thank Bálint Nagy, Alessandro Venturino, Ryan
347 John A. Cubero, Marco Benevento and all members of the Siegert group for constant
348 feedback on the project and manuscript.

349

350 **<u>Figure legends</u>**

351

352 **Figure 1. Mitochondrial networks in retinal microglia of the inner plexiform layer**
353 **(IPL).**

354 (**A**-**F**) Mouse models for mitochondrial visualization (**A**-**C**) and UCP2 (uncoupling protein 2)
355 knockout (**D**-**F**). (**A**, **D**) Schematic of mouse models. *Cx3cr1*^{CreERT2}/Pham$^{fl/fl}$ for selective
356 mitochondria-labeling in microglia (**A**) or combined with UCP2 knockout
357 (*Cx3cr1*$^{CreERT2/+}$/Pham$^{fl/fl}$/UCP2$^{fl/fl}$) (**D**). Upon tamoxifen injection for three consecutive days
358 in adult mice, *Cx3cr1*^{CreERT2}-expressing microglia excise the stop cassette in Pham$^{fl/fl}$ (**A**,
359 μG^{mito}) or in addition, exon 3 and 4 of UCP2 in Pham$^{fl/fl}$/UCP2$^{fl/fl}$ (**D**, μG^{mito}UCP2^{KO}) to
360 induce mito-Dendra2 (green) expression and UCP2 knockout. (**B**, **E**) Overview image of
361 immunostained microglia (IBA1, magenta) in the inner plexiform layer (IPL) expressing the
362 mitochondrial label (Dendra2, green) in retinal wholemounts for μG^{mito} (**B**) and
363 μG^{mito}UCP2^{KO} (**E**). Scale bar: 50 μm. (**C**, **F**) Zoom-in (dashed orange line) of a single cell
364 acquisition of immunostained IPL microglia (IBA1, magenta) expressing mitochondria label
365 Dendra2 from μG^{mito} (**C**) and μG^{mito}UCP2^{KO} (**F**) retinas. Below: Zoom-out of the
366 corresponding 3D-surface rendering of IBA1 microglia (magenta outline) and Dendra2
367 mitochondria (green). Dashed blue circle: Location of cell soma. Scale bar: zoom-in: 5 μm,

368 3D-surface: 10 µm. (**G-I**) Mitochondrial parameters. Boxplot minimum and maximum:
369 InterQuartile Range (IQR) around median (center line). Whiskers: 1.5 IQRs. Black diamond:
370 outliers outside of 1.5 IQRs. Each overlaid point represents data point of a single microglia.
371 Filled circle: female, filled diamond: male. μG^{mito} naïve: n = 18 cells, 5 retinas;
372 $\mu G^{mito}UCP2^{KO}$: n = 21 cells, 4 retinas. (**G**) Mitochondrial network connectivity determined
373 by median mitochondrial volume of all organelles (left, Student's t-test: $p = 0.7710$) and
374 number of organelles within a single cell (right, Student's t-test: $p = 0.7187$).
375 (**H**) Percentage of mitochondrial volume per microglial volume. Wilcoxon rank sum test: $p =$
376 0.6121. (**I**) Percentage of total mitochondrial volume localized within the perinuclear region
377 (10 µm radius from center soma point). Student's t-test: $p = 0.4908$.
378 $^{n.s.}$ $p > 0.05$: not significant.
379
380 **Figure 2. *Ucp2* is upregulated upon ONC and accompanied by mitochondrial network**
381 **alterations in responsive μG^{mito} microglia.**
382 (**A**) Schematic of optic nerve crush (ONC). Forceps induces unilateral damage (red) to retinal
383 ganglion cell's (RGC) axonal projections (orange) posterior to the optic disc. (**B**) Left, retinal
384 side-view schematic. OPL, outer plexiform layer. IPL, inner plexiform layer. GCL, ganglion
385 cell layer. Right, overview confocal image of immunostained IPL microglia (IBA1, magenta)
386 of C57BL6/J in naïve (left) and 5 days after ONC (right) condition. Scale bar: 30 µm. (**C**)
387 Boxplot of relative *Ucp2* transcript expression from Dendra2^{+}-FACSorted retinal microglia
388 in naïve or 5 days ONC condition. Boxplot minimum and maximum: InterQuartile Range
389 (IQR) around median (center line). Whiskers: 1.5 IQRs. Black diamond: outliers outside of
390 1.5 IQRs. Filled circle: female, filled diamond: male. Naïve: grey. ONC: blue. Wilcoxon rank
391 sum test: $p < 0.0458$. (**D-O**) Comparison of microglial and mitochondrial response in μG^{mito}
392 in naïve (grey) and 5 days after ONC (blue). (**D- I**) A representative IBA1-immunostained
393 microglia for naïve (**D-F**) or 5 days ONC (**G-I**) depicting 3D-traced filaments (**D**, **G**) or 3D-
394 surface renderings of IBA1 (magenta outline) and CD68 (blue **E**, **H**) or mitochondria (green,
395 **F**, **I**). Dashed blue circle: Location of cell soma. Scale bar: 10 µm. (**J**) Line plot for mean
396 number of Sholl intersections per radial distant from the soma (in µm) with 95% confidence
397 interval band. Linear regression analysis: $p < 0.0001$. (**K-O**) Boxplot minimum and
398 maximum: InterQuartile Range (IQR) around median (center line). Whiskers: 1.5 IQRs.
399 Black diamond points: outliers outside 1.5 IQRs. Each overlaid point represents data point of
400 a single microglia. Filled circle: female, filled diamond: male. $\mu G^{mito}_{naïve}$, n= 18 cells, 5

401 retinas; $\mu G^{mito}{}_{ONC}$, n = 14 cells, 6 retinas. (**K**) Percentage of total CD68 volume per microglia
402 volume. Wilcoxon rank sum test: $p < 0.0001$.
403 (**L**) Percentage of total CD68 volume localized in the peripheral processes of microglia (>10
404 µm radius from center soma point). Wilcoxon rank sum test: $p = 0.0021$. (**M**) Mitochondiral
405 network connectivity determined by median mitochondrial volume of all organelles (left,
406 Welch's t-test: $p < 0.0001$) and number of organelles within a single cell (right, Welch's t-
407 test: $p = 0.0004$). (**N**) Percentage of mitochondrial volume per microglial volume. Student's t-
408 test: $p = 0.0126$. (**O**) Percentage of total mitochondrial volume localized within the
409 perinuclear region (<10 µm radius from center soma point). Wilcoxon rank sum test: $p <$
410 0.0001. * $p < 0.05$, ** $p < 0.01$, *** $p < 0.001$.
411
412 **Figure 3. $\mu G^{mito}UCP2^{KO}$ microglia exhibit ONC-induced mitochondrial and microglial**
413 **alterations**
414 (**A**-**L**) Comparison of microglial and mitochondrial response in $\mu G^{mito}UCP2^{KO}$ in naïve
415 (grey/sand) and 5 days after optic nerve crush (ONC, gold). (**A**-**I**) A representative IBA1-
416 immunostained microglia for naïve (**A**, **D**, **H**) or 5 days ONC (**B**, **E**, **I**) depicting 3D-traced
417 filaments (**A**, **B**) or 3D-surface renderings of IBA1 (magenta outline) and CD68 (blue **D**, **E**)
418 or mitochondria (green, **H**, **I**). Dashed blue circle: location of cell soma. Scale bar: 10 µm.
419 (**C**) Line plot for mean number of Sholl intersections per radial distant from the soma (in µm)
420 with 95% confidence interval band. Linear regression analysis: $p < 0.0001$. (**F**-**L**) Boxplot
421 minimum and maximum: InterQuartile Range (IQR) around median (center line). Whiskers:
422 1.5 IQRs. Black diamond points: outliers outside 1.5 IQRs. Each overlaid point represents
423 data point of a single microglia. Filled circle: female, filled diamond: male.
424 $\mu G^{mito}UCP2^{KO}{}_{naïve}$, n = 21 cells, 4 retinas; $\mu G^{mito}UCP2^{KO}{}_{ONC}$, n = 22 cells, 4 retinas. (**F**)
425 Percentage of total CD68 volume per microglia volume. Wilcoxon rank sum test: $p = 0.0004$.
426 (**G**) Percentage of total CD68 volume localized in the peripheral processes of microglia (>10
427 µm radius from center soma point). Student's t-test: $p = 0.9277$. (**J**) Mitochondiral network
428 connectivity determined by median mitochondrial volume of all organelles (left, Welch's t-
429 test: $p = 0.0008$) and number of organelles within a single cell (right, Welch's t-test: $p =$
430 0.0693). (**K**) Percentage of mitochondrial volume per microglial volume. Wilcoxon Rank
431 Sum test: $p = 0.0093$.
432 (**L**) Percentage of total mitochondrial volume localized within the perinuclear region (<10
433 µm radius from center soma point). Student's t-test: $p < 0.0001$. * $p < 0.05$, ** $p < 0.01$, ***
434 $p < 0.001$, $^{n.s.}$ $p > 0.05$: not significant.

435

436 **Figure 4. Sex-specific microglial response in μG^{mito}UCP2^{KO} after ONC**

437 Principle component analysis (PCA) of microglia from μG^{mito} and μG^{mito}UCP2^{KO} condition
438 in naïve (**A**-**C**) and 5 days after ONC (**D**-**F**). The first two principle components (PC) are
439 visualized. Each grey dot represents a single microglial profile defined by the following
440 seven parameters: microglial Sholl index, CD68 volume, CD68 localization, median
441 mitochondrial volume, number of mitochondria, % mitochondrial volume per microglia, %
442 mitochondrial volume perinuclear obtained from aforementioned condition and environment.
443 PC1 and PC2 describe 45% and 22% of the explained variance across the population,
444 respectively. Each subpanel highlights the following comparisons: (**A**) Naïve microglial
445 profiles for μG^{mito} (grey) and μG^{mito}UCP2^{KO} (sand). (**B**-**C**) Naïve microglial profiles in male
446 (green) and female (magenta) for μG^{mito} (**B**) and in sand for μG^{mito}UCP2^{KO} (**C**). Dashed
447 outline: Reference of distribution shown in (**A**). (**D**) ONC microglial profiles for μG^{mito} (blue)
448 and μG^{mito}UCP2^{KO} (gold). (**E**) Naïve microglial profiles in male (green) and female
449 (magenta) for μG^{mito} (**E**) and μG^{mito}UCP2^{KO} (**F**). Dashed outline: Reference of distribution
450 shown in (**D**).

451

452 **Figure 5. Male μG^{mito}UCP2^{KO} microglia exhibit hyperfused mitochondrial network**
453 **after ONC**

454 (**A**-**C**) Principle component analysis (PCA) of microglia using mitochondrial parameters
455 from μG^{mito} (blue) and μG^{mito}UCP2^{KO} (gold) in ONC environment. The first two principle
456 components (PC) are visualized. Each grey dot represents a single microglial profile defined
457 by the following four parameters: median mitochondrial volume, number of mitochondria, %
458 mitochondrial volume per microglia, % mitochondrial volume perinuclear. PC1 and PC2
459 describe 46% and 33% of the explained variance across the population, respectively. Each
460 subpanel highlights the following comparisons: (**A**) ONC microglial profiles for μG^{mito} (blue)
461 and μG^{mito}UCP2^{KO} (gold). (**B**-**C**) ONC microglial profiles in male (green) and female
462 (magenta) for μG^{mito} (**B**) and for μG^{mito}UCP2^{KO}. Dashed outline: Reference of distribution
463 shown in (**A**). (**D**-**E**) Representative 3D-surface renderings of IBA1 (magenta outline) and
464 mitochondria (statistics-based volume spectral coloring) from ONC-induced μG^{mito} (top) and
465 μG^{mito}UCP2^{KO} (bottom) in male (**D**) or female (**E**) microglia. Stripplot of the entire
466 population of mitochondrial organelles in each cell for all conditions and environments. Each
467 dot represents one organelle. Each hue: One microglia within a condition. Volume spectrum:
468 0 μm^3 (blue) – 10 μm^3 (red).

469

470 **Figure 6. Sex-specific, transient microglial stress response affects RGC susceptibility in**
471 **UCP2^{KO} mice**

472 (**A**) Principle component analysis (PCA) of microglia using mitochondrial parameters from
473 μG^{mito} and μG^{mito}UCP2^{KO} in ONC condition. The first two principle components (PC) are
474 visualized. Each dot (grey) represents a single microglial profile defined by the following
475 four mitochondrial parameters: median mitochondrial volume, number of mitochondria, %
476 mitochondrial volume per microglia, % mitochondrial volume perinuclear. PC1 and PC2
477 describe 41% and 32% of the explained variance across the population, respectively. Each
478 subpanel highlights the following comparisons: (**A**) ONC microglia profiles for male (green)
479 and female (magenta) at 5 days (open circles) and 14 days (filled circles) after injury in ONC
480 microglia profiles for μG^{mito}UCP2^{KO} (left, gold) or μG^{mito} (right, blue). (**B**) Stripplot of all
481 mitochondrial organelles in each cell for all conditions and environments. Each dot represents
482 one organelle. Each hue: separate microglia within a condition. (**C**) Schematic of genes
483 evaluated for RT-qPCR analysis. OXPHOS: oxidative phosphorylation. (**D**-**F**) Principle
484 component analysis (PCA) of microglia using metabolic and stress genes from μG^{mito} and
485 μG^{mito}UCP2^{KO} conditions in naïve or ONC environments from male (top) or female (bottom).
486 The first two principle components (PC) are visualized. Each dot (filled diamond: male, filled
487 circle: female, grey) represents 100 FACSorted microglia from one retina defined by the ΔCq
488 values of *Nrf1, Pgc1-α, Hif1-α, Sod1, Cd68*. PC1 and PC2 describe 42% and 25% of the
489 explained variance across the population, respectively. An enlarged summary PC point for
490 each condition and environment is overlaid on the plot, with green (male) or magenta
491 (female) arrows depicting the overall shift between the following highlighted conditions
492 compared in each subpanel: (**D**-**F**) Male (top, filled diamond) and female (bottom, filled
493 circle) profiles for naive μG^{mito} (grey) or μG^{mito}UCP2^{KO} (sand) (**D**), naive μG^{mito} (grey) or
494 ONC μG^{mito} (blue) (**E**), and μG^{mito}UCP2^{KO} (sand) or ONC μG^{mito}UCP2^{KO} (gold) (**F**). (**G**-**H**)
495 Percentage of retinal ganglion cells (RGC) remaining (% of naïve control) after ONC in
496 μG^{mito} at 5 days (blue) or 14 days (dark blue) and μG^{mito}UCP2^{KO} at 5 days (gold) or 14 days
497 (orange) in for male (**G**) or female (**H**). n, number of retinas. **G**, ♂μG$_{naïve}$, n = 5; day 5, n = 4;
498 day 14, n = 3. ♂UCP2$^{KO}_{naïve}$, n = 6; day 5, n = 4; day 14, n = 3. One-way ANOVA, $p <$
499 0.0001. Selected Tukey's post-hoc comparison: Day 5 ONC ♂μG^{mito} *vs.* ♂μG^{mito}UCP2^{KO} $p =$
500 0.0081; Day 14 ONC ♂μG^{mito} *vs.* ♂μG^{mito}UCP2^{KO} $p = 0.9000$. **H**, ♀μG$_{naïve}$, n = 6; day 5, n =
501 4; day 14 = 2. ♀UCP2$^{KO}_{naïve}$, n = 6; day 5, n = 4: day 14 = 2 retinas. Kruskal-Wallis, $p =$
502 0.044. Selected Dunn's post-hoc comparison with Bonferonni p-adjustment: Day 5 ONC

503 ♀μG^{mito} *vs.* ♀μG^{mito}UCP2^{KO} p = 1.000; Day 14 ONC ♀μG^{mito} *vs.* ♀μG^{mito}UCP2^{KO} p = 1.000.
504 ** $p < 0.01$. $^{n.s.}$ $p > 0.05$: not significant
505
506 **Figure S1. Selective expression and knockout of UCP2 in retinal microglia**
507 (**A**-**B**) Relative fold change expression level of mitochondrial-associated genes (**A**) and *Ucp2*
508 (**B**) among retinal cell types. Plotted from available data in *Siegert et. al*. (Siegert et al.,
509 2012). Purple and blue: high and low normalized expression value, respectively. PR:
510 photoreceptors, H: horizontal cells, BP: bipolar cells, Am: amacrine cells, RGC: retinal
511 ganglion cells, μG: microglia. (**C**) Timeline for tamoxifen administration to induce mito-
512 Dendra2 expression in microglia used for FACSorting. FACS: fluorescence activated cell
513 sorting. (**D**) Relative *Ucp2* transcript expression from tamoxifen-induced μG^{mito} or
514 μG^{mito}UCP2^{KO} FACSorted- microglia from the retina. Wilcoxon rank sum test: p = 0.0004.
515 *** $p < 0.001$. (**E**) Experimental timeline for primary murine mixed glia cultures to obtain
516 microglia-enriched cultures for protein analysis. P0-P3: postnatal day 0 to 3. 4-OHT: 4-
517 hydroxytamoxifen. Next: IBA1-immunostained mixed glial culture at day 10 before
518 trypsination. Scale bar: 50 μm. (**F**) Western blot analysis of UCP2 protein expression (top) or
519 β-actin loading control (bottom) in primary microglia of either *Cx3cr1*$^{CreERT2/+}$ or
520 *Cx3cr1*$^{CreERT2/+}$/UCP2$^{fl/fl}$ vehicle or 4-OHT (n = 1). kDa, kilodaltons. (**G**) Quantification of
521 UCP2 band intensity.
522
523 **Figure S2. Time course of optic nerve crush (ONC)-induced retinal ganglion cell death**
524 **and microglial response in C57BL6/J mice**
525 (**A**) Representative retinal ganglion cell distribution in wholemount retina immunostained for
526 RBPMS (RNA binding protein with multiple splicing) at naïve, or 1, 5, 14 days after ONC.
527 Scale bar: 30 μm. (**B**-**I**) Response of microglia after ONC in the inner (IPL, **B**-**E**) and the
528 outer plexiform layer (OPL, **F**-**I**). (**B**, **F**) Representative images of immunostained microglia
529 (magenta, IBA1) in naïve, or 1, 5, and 14 days after either ONC (top) or sham (bottom)
530 surgery. Scale bar: 30 μm. (**C**, **G**) Lineplots of the mean number of Sholl intersections at
531 increasing radii from the microglia soma (in μm). 95% confidence interval band. Naïve: grey.
532 Sham: green. ONC: blue. n = cells/retina. **C**, IPL: naïve, n = 161/8; ONC day 1, n = 26/3;
533 ONC day 5, n = 152/4; ONC day 14, n = 90/4; Sham day 1, n = 58/2; Sham day 5, n = 44/4;
534 Sham day 14, n = 15/2. **G**, OPL: naïve, n= 159/8; ONC day 1, n = 29/2; ONC day 5, n =
535 47/3; ONC day 14, n = 66/4; Sham day 1, n = 45/4; Sham day 5, n = 42/3; Sham day 14, n =
536 12/2 retinas. (**D**, **H**) Representative images of CD68 immunostaining (white) in microglia

537 from naïve or 5 days after ONC highlighted with dashed, colored borders in (**B**, **F**). Arrows:
538 CD68 labeling. Scale bar: 10 µm. (**E**, **I**) Percent CD68 volume in total microglia volume.
539 Naïve: grey. Sham: green. ONC: blue. Boxplot minimum and maximum: InterQuartile Range
540 (IQR) around median (center line). Whiskers: 1.5 IQRs. Black diamond: outliers outside of
541 1.5 IQRs. Filled circle: one image. n= 3-4 retinas, 1 image per retina. **E**, IPL: Naïve *vs.* ONC
542 Day 5, Student's t-test: $p = 0.0353$. Naïve *vs.* Sham Day 5, Student's t-test: $p = 0.9438$. **I**,
543 OPL: One-way ANOVA: $p = 0.6282$. * $p < 0.05$. $^{n.s.}$ $p > 0.05$: not significant.
544
545 **Figure S3. Individual mitochondrial parameters and PC loadings**
546 (**A**) Table of principal component (PC) loadings using mitochondrial, CD68, and Sholl index
547 parameters from **Figure 4**. Orange outline: Highest loadings for PC1. Green outline: Highest
548 loadings for PC2. (**B-D**) Principle component analysis (PCA) of microglia using Sholl index
549 and CD68 parameters from μG^{mito} (blue) and $\mu G^{mito}UCP2^{KO}$ (gold) in ONC environment. The
550 first two principle components (PC) are visualized. Each dot (grey) represents a single
551 microglial profile defined by the following three parameters: microglial Sholl index, CD68
552 volume, CD68 localization. PC1 and PC2 describe 58% and 29% of the explained variance
553 across the population, respectively. Each subpanel highlights the following comparisons:
554 (**B**) ONC microglial profiles for μG^{mito} (blue) and $\mu G^{mito}UCP2^{KO}$ (gold). (**C-D**) ONC
555 microglial profiles in male (green) and female (magenta) for μG^{mito} (**C**) and $\mu G^{mito}UCP2^{KO}$
556 (**D**) Dashed outline: reference of distribution shown in (**B**). (**E**) Table of principal component
557 (PC) loadings from PCA using four mitochondrial parameters (median mitochondrial
558 volume, number of mitochondria, % mitochondrial volume per microglia, % mitochondrial
559 volume perinuclear) from **Figure 5A-C**. Green outline: Highest PC loading in PC2.
560 (**F-H**) Mitochondrial parameters. Boxplot minimum and maximum: InterQuartile Range
561 (IQR) around median (center line). Whiskers: 1.5 IQRs. Black diamond: outliers outside 1.5
562 IQRs. Each overlaid point represents data point of a single microglia. n = cells/retina.
563 ♂$\mu G^{mito}_{naïve}$ (grey), n = 11/2; ♀$\mu G^{mito}_{naïve}$ (grey), n = 7/3; ♂μG^{mito}_{ONC} (blue), n = 7/4;
564 ♀μG^{mito}_{ONC} (blue), n = 7/2; ♂$\mu G^{mito}UCP2^{KO}_{naïve}$ (sand), n = 10/2; ♀$\mu G^{mito}UCP2^{KO}_{naïve}$ (sand),
565 n = 11/2; ♂$\mu G^{mito}UCP2^{KO}_{ONC}$ (gold), n = 10/2; ♀$\mu G^{mito}UCP2^{KO}_{ONC}$ (gold), n = 12/2.
566 (**F**) Mitochondrial network connectivity determined by median mitochondrial volume of all
567 organelles (left, one-way ANOVA: $p < 0.0001$, Selected Tukey's post-hoc comparisons:
568 ♂$\mu G^{mito}UCP2^{KO}_{naïve}$ *vs.* ♂$\mu G^{mito}UCP2^{KO}_{ONC}$, $p = 0.4917$; ♀$\mu G^{mito}UCP2^{KO}_{naïve}$ *vs.*
569 ♀$\mu G^{mito}UCP2^{KO}_{ONC}$, $p = 0.0094$) and number of organelles within a single cell (right,
570 Kruskal-wallis test: $p = 0.0004$. Selected Dunn's post-hoc comparisons with Bonferonni p-

571 adjustment: ♂μG^{mito}UCP2^{KO}$_{naïve}$ *vs.* ♂μG^{mito}UCP2^{KO}$_{ONC}$, p = 1.0; ♀μG^{mito}UCP2^{KO}$_{naïve}$ *vs.*
572 ♀μG^{mito}UCP2^{KO}$_{ONC}$, p = 1.0). (**G**) Percentage of mitochondrial volume per microglial
573 volume. Kruskal-wallis test: p = 0.0006. Selected Dunn's post-hoc comparisons with
574 Bonferonni p-adjustment: ♂μG^{mito}$_{naïve}$ *vs.* ♂μG^{mito}UCP2^{KO}$_{ONC}$, p = 0.0011;
575 ♀μG^{mito}UCP2^{KO}$_{navie}$ *vs.* ♂μG^{mito}UCP2^{KO}$_{ONC}$, p = 0.0005. (**H**) Percentage of total
576 mitochondrial volume localized within the perinuclear region (10 μm radius from center
577 soma point). One-way ANOVA: p < 0.0001. Selected Tukey's post-hoc comparisons:
578 ♂μG^{mito}$_{naive}$ *vs.* ♂μG^{mito}$_{ONC}$ p = 0.0032. ** p < 0.01, *** p < 0.001, $^{n.s.}$ p > 0.05: not
579 significant. For other post-hoc comparisons see **Table S3**.
580
581 **Figure S4. PCA comparison for naïve environment and relative transcript expression**
582 (**A**) PCA from **Figure 6A** highlighting comparison between naïve conditions (left) for in
583 μG^{mito} (grey) or μG^{mito}UCP2^{KO} (sand) and days 5 and 14 after ONC condition (right) in
584 μG^{mito} (blue) or μG^{mito}UCP2^{KO} (gold). (**B**) Table of principal component (PC) loadings from
585 PCA using the metabolic (*Nrf1, Pgc1α, Hif1α*) and stress (*Sod1, Cd68*) genes in **Figure 6**.
586 (**C**) PCA from **Figure 6** highlighting comparison of male (filled diamond) and female (filled
587 circle) profiles for naïve μG^{mito} (left, grey) or naïve μG^{mito}UCP2^{KO} (right, sand). (**D-E**)
588 Boxplot minimum and maximum: InterQuartile Range (IQR) around median (center line).
589 Whiskers: 1.5 IQRs. Black diamond points: outliers outside 1.5 IQRs. Each overlaid point
590 represents data point of a single microglia. Filled circle: female, filled diamond: male. n,
591 number of retinas. μG^{mito}$_{naïve}$: n= ♂9, ♀9; μG^{mito}$_{ONC}$: n = ♂4, ♀3; μG^{mito}UCP2^{KO}$_{naïve}$: n = ♂3,
592 ♀4; μG^{mito}UCP2^{KO}$_{ONC}$: n = ♂3, ♀5. (**D-E**) Fold change of *Pgc1α, Nrf1, Hif1α* in conditions
593 and environments for males (**D**) and females (**E**) normalized to their corresponding naïve
594 μG^{mito}. ♂*Pgc1α*: Kruskal-Wallis test, p = 0.0075 with shown selected Dunn's post-hoc
595 comparison with Bonferonni p-adjustment: μG^{mito}$_{naive}$ *vs.* μG^{mito}$_{ONC}$ p = 0.0393; μG^{mito}$_{naive}$ *vs.*
596 μG^{mito}UCP2^{KO}$_{ONC}$ p = 0.0322. ♂*Nrf1*: Kruskal-Wallis test, p = 0.0078 with shown selected
597 Dunn's post-hoc comparison with Bonferonni p-adjustment: μG^{mito}$_{naive}$ *vs.* μG^{mito}$_{ONC}$ p =
598 0.0071. ♂*Hif1α*: One-way ANOVA, p = 0.2400. ♀*Pgc1α*: Kruskal-Wallis test, p = 0.0706.
599 ♀*Nrf1*: Kruskal-Wallis test, p = 0.1620. ♀*Hif1-α*: One-way ANOVA, p = 0.2323. (**F**) Fold
600 change of *Sod1* (left) and *Cd68* (right) across sexes. Left, *Sod1*: One-way ANOVA, p =
601 0.0181 with selected Tukey's post-hoc comparison: μG^{mito}$_{naive}$ *vs.* μG^{mito}UCP2^{KO}$_{ONC}$ p =
602 0.0398. Right, *Cd68*: Kruskal-Wallis test: p = 0.0001 with selected Dunn's post-hoc
603 comparison with Bonferonni p-adjustment: ♂μG^{mito}$_{naive}$ *vs.* ♂μG^{mito}$_{ONC}$ p = 0.0205;

604 ♂μG^{mito}_{naive} *vs.* ♂$\mu G^{mito}UCP2^{KO}_{ONC}$ $p = 0.0184$. * $p < 0.05$, ** $p < 0.05$, $^{n.s.}$ $p > 0.05$: not
605 significant. For other post-hoc comparisons see **Table S3**.
606
607 **Table S1.** Primer sequences.
608 **Table S2.** Antibody table.
609 **Table S3.** Statistical analysis.
610
611 **Materials and Methods**
612
613 *Animals*
614 Animal housing and procedures were approved by the "Bundesministerium für Wissenschaft,
615 Forschung und Wirtschaft (bmwfw) Tierversuchsgesetz 2012, BGBI. I Nr. 114/2012 (TVG
616 2012) under the number GZ: 2021-0.607.460. Mice were housed in a 12 hour light-dark cycle
617 in individually ventilated cages in a controlled environment (room temperature 22 ± 1 °C;
618 relative humidity 55 ± 10 %) with access to standard diet (rat/mouse maintenance diet
619 (V1534-300) or mouse breeding diet (V1124-300), ssniff Spezialitäten GmbH) and
620 autoclaved water provided *ad libitum* in the ISTA Preclinical facility. Founder mouse strains
621 were obtained from Jackson Laboratories and backcrossed to C57Bl6/J (#000664)
622 background for at least 10 generations: *Cx3cr1*^{CreERT2} (#020940), PhAM$^{fl/fl}$ (#018385),
623 UCP2$^{fl/fl}$ (#022394). Throughout the manuscript μG^{mito} refers to *Cx3cr1*$^{CreERT2/+}$/Pham$^{fl/fl}$,
624 while $\mu G^{mito}UCP2^{KO}$ refers to *Cx3cr1*$^{CreERT2/+}$/Pham$^{fl/fl}$/UCP2$^{fl/fl}$. For UCP2 protein knockout
625 primary microglia culture experiments (**Figure S1E-G**) and retinal ganglion cell counting
626 experiments (**Figure 6C**), mice did not contain the Dendra2 mitochondria label, and instead
627 were *Cx3cr1*$^{CreERT2/+}$/ and *Cx3cr1*$^{CreERT2/+}$/UCP2$^{fl/fl}$.
628
629 *Tamoxifen administration for Cre-induced recombination*
630 Tamoxifen (Sigma Aldrich, T5648-5G) was dissolved in corn oil (Sigma Aldrich, C8267-
631 500ML) at a concentration of 20 mg/mL and sonicated for 40 minutes. Freshly prepared
632 tamoxifen was administered via intraperitoneal injection daily (150mg/kg) for three days.
633 The animals did not show any abnormal behavior or discomfort after gene knockout. All
634 experimental groups (μG^{mito} and $\mu G^{mito}UCP2^{KO}$, naïve and ONC) were tamoxifen-injected for
635 two reasons; first, expression of the Dendra2 mitochondria label is only possible after Cre
636 recombinase excision of the stop cassette and second, *Cx3Cr1*^{CreERT2} reporter lines have been
637 shown to include some 'leakiness', *i.e.* tamoxifen-independent *Cre* recombination (Van Hove

638 et al., 2020). *Cx3Cr1*^{CreERT2} mice also express CreERT2 in monocyte populations, therefore
639 to ensure no interference from UCP2^{KO} circulating monocytes, ONC experiments were
640 performed at least three weeks after tamoxifen induction when monocyte populations have
641 turned over (Goldmann et al., 2013). This also provided sufficient time for adaptation of
642 microglia to the UCP2 loss conditions and clearance of all tamoxifen metabolites (Jahn et al.,
643 2018).
644
645 *Optic nerve crush (ONC) procedure*
646 Mice were anesthetized in an induction chamber with 5% (v/v) isoflurane (Zoetis) supplied
647 with oxygen at a flow rate of 0.6 L/min. After lack of a foot pinch reflex, mice were
648 maintained at 2.5% (v/v) isoflurane applied through a nose cone while on a heating pad to
649 maintain body temperature at 37ºC. Proparacaine hydrochloride 0.5% ophthalmic eye drops
650 (Ursapharm Arzneimittel GmbH) were applied to numb the eyes, and subcutaneous injection
651 of 5mg/kg Metacam alleviated pain (Meloxacam, Boehringer Ingelheim). The lateral canthus
652 was de-vascularized by clamping with a hemostat (Fine Science Tools) for 10 seconds. Using
653 a Leica dissection microscope, a lateral canthotomy allowed visualization of the posterior
654 pole. While firmly holding the conjunctiva with a jeweler forceps, the conjunctiva was cut
655 perpendicular to the posterior pole. The surrounding muscle was carefully dissected as to not
656 puncture the vascular plexus. The optic nerve was pinched 1mm from the posterior pole for 4
657 seconds using a curved N7 self-closing forceps (Dumont). Triple antibiotic ointment was
658 applied to the eye directly after the surgery to prevent infection.
659
660 *Primary glial culture*
661 Mixed glia culture were prepared from the published protocol by *Bronstein et al*. (Bronstein
662 et al., 2013). Cortices from 3-5 murine pups aged P0-P2 were dissected under a sterile
663 ventilation hood in ice-cold Hank's buffered saline (ThermoFisher, #14025-050) and digested
664 in 0.05% (v/v) Trypsin + 1X EDTA (ThermoFisher, #25300-054) for 15 minutes at 37°C.
665 The trypsinization was stopped with the addition of serum-containing medium (DMEM, 10%
666 (v/v) heat-inactivated FBS, 1% (v/v) Penicillin/Streptomycin, 1% (v/v) Non-essential amino
667 acids (Sigma-Aldrich, M7145-100ML)). Cells were pelleted at 500xg for 5 min, washed one
668 time with serum-containing medium, then passed through a 40µm cell strainer (Szabo-
669 Scandic, #352340). For Western blotting, the resulting cell suspension was plated onto T75
670 cell culture flasks (TPP, #Z707503). The culture medium was replaced at day 3 and day 10.
671

672 *Primary microglia isolation*
673 Two T75 flasks containing mixed primary glia cultures prepared in tandem were treated with
674 1µM 4-hydroxy tamoxifen (Sigma-Aldrich, SML1666-1ML) or vehicle at day 10. Three days
675 later, microglia were isolated using mild trypsinization (0.8mM $CaCl_2$ in 1xTrypsin-EDTA,
676 ThermoFisher #25300-054) is added to the flask after a washing step with pre-warmed 1X
677 PBS to remove inhibiting serum, then incubate at 37ºC for 10-20 minutes, or until the non-
678 microglial cells have just lifted from the flask forming a floating layer. The floating cells
679 were collected with the supernatant, spun down at 10,000xg, washed once with 1X PBS,
680 pelleted and snap-frozen. The microglia remaining on the flask were overlaid with 5ml 1X
681 PBS, removed using a cell scraper, pelleted, and snap-frozen.
682
683 *Western blotting*
684 Total cellular protein isolation, production of recombinant UCP2 in *E. coli*, and western blot
685 (WB) was performed as described previously (Rupprecht et al., 2012, 2014). For WB
686 analyses 10 µg of total protein were loaded on the SDS-gel, 1 ng of recombinant UCP2 was
687 used as positive control for anti-UCP2 antibody detection. To ensure blotting homogeneity to
688 nitrocellulose membranes, Ponceau S staining was performed. To relate UCP2 expression to
689 loading control, the membranes were stripped, re-blocked and incubated with β-actin. The
690 affinity purified antibody against the N-terminal sequence of mouse UCP2
691 (VGFKATDVPPTATVKF) was designed and evaluated in the Pohl laboratory (Rupprecht et
692 al., 2012). Peptide synthesis, rabbit immunization and affinity purification were performed by
693 PINEDA Antibody-service GmbH (Berlin, Germany). The production of recombinant murine
694 UCP2, used as positive control, was performed as described in (Žuna et al., 2021).
695
696 *Microglia isolation and sample preparation for fluorescence-activated cell sorting (FACS)*
697 Adult animals expressing the mito-Dendra2 tag were anesthetized with isoflurane and
698 decapitated. Retinas were immediately explanted and dissected in 1X PBS on ice. Each retina
699 was transferred to a 1.5ml Eppendorf low-adhesion tube filled with the 800µl digestion buffer
700 (1:8:1 Cysteine/EDTA solution (2.5mM Cysteine, 0.5mM EDTA (ethylenediaminetetraacetic
701 acid) in HBSS, 10mM HEPES (4-(2-hydroxyethyl)-1-piperazineethanesulfonic acid) in
702 HBSS, and 10mg/ml Papain, Roche #10108014001), incubated at 37ºC for 10 minutes, then
703 centrifuged for 2.5 min at 240xg. Samples were transferred on ice, the supernatant was
704 discarded and 800µl 1mM EDTA in HBSS + 2% (v/v) FBS added. After two washes with

705 1mM EDTA in HBSS + 2% (v/v) FBS, the digested tissue was triturated 10-15 times with a
706 pulled glass pipette, then filtered through a 70 µm strainer.
707
708 *Fluorescent activated cell sorting (FACS)*
709 FACS was performed using a SONY SH800SFP equipped with a 100 µm nozzle and sorting
710 speed of approximately 8,000 events per second in normal purity mode. Microglia were gated
711 from the population by setting the forward and side scatter and by the fluorescence of the
712 mito-Dendra2 tag. From each retina, 100 microglia were sorted and immediately collected in
713 one well of a 96-well plate (Eppendorf) filled with 5 µl cold lysis buffer from the NEBNext®
714 Single Cell/Low Input cDNA Synthesis & Amplification Module (New England Bio Labs,
715 #E6421L). After the sorting, the plate was shortly spun down to ensure all cells were
716 collected at the bottom of the well and was immediately processed for cDNA synthesis.
717
718 *cDNA synthesis*
719 Sorted microglia were processed with the NEBNext® Single Cell/Low Input cDNA
720 Synthesis & Amplification Module (New England Bio Labs, #E6421L) according to the
721 manufacturer's protocol.
722
723 *Reverse transcription quantitative real-time PCR and gene expression analysis*
724 Primers (**Table S1**) were designed with the free PrimerQuest Tool from Integrated DNA
725 Technologies (https://eu.idtdna.com/PrimerQuest/Home/Index). To ensure the target
726 sequence of each primer, primers were blasted (https://www.ncbi.nlm.nih.gov/tools/primer-
727 blast/). Their self-complementarity and folding probability were investigated using the
728 UNAFold Web server (http://www.unafold.org/). Primer efficiencies were validated from the
729 slope of four to five serial 1:4 dilutions of cDNA template according to equation (1). Primers
730 with efficiencies between 90-110% were used.

731 $$(1)\ Efficiency = ((2^{\wedge -\frac{1}{Slope}}) - 1) * 100$$

732
733
734 For gene expression analysis, RT-qPCR (Luna® Universal qPCR Master Mix; New England
735 BioLabs; M3003L) was performed in 384-well plates (Bio-Rad; HSR4805) on a Roche
736 Lightcycler 480 according to the manufacturer's manual. Total reaction volume was 10µl
737 containing 1µl of 1:10 diluted cDNA as template and a final concentration of 0.25µM for

each primer. Cycle conditions were 60 seconds at 95°C for initial denaturation, followed by 40 cycles of denaturation (15 seconds; 95°C) and annealing/extension (30 seconds; 60°C). Each run was completed with a melting curve analysis to confirm amplification of only one amplicon. Each PCR reaction was run in triplicate from which a mean Cq value was calculated and used for further analysis.

Analysis of RT-qPCR results

Fold change differences between each condition and μG^{mito}_{naive} were calculated according to delta-delta Ct method (Schmittgen and Livak, 2008). dCq values were obtained by normalizing mean Cq values to the reference housekeeping gene (GAPDH) measured within the same experiment (Equation 2). ddCq values were then calculated by normalizing dCq values to the respective control condition (μG^{mito}_{naive}) within each experimental repetition (Equation 3). Fold changes were obtained by transforming ddCq values from log2-scale to linear scale (Equation 4). These fold changes were used for data visualization. Exclusion criteria were based on IBA1 and GFAP fold change expression to determine purity of cell isolation, which would indicate substantial contamination from astrocytes and müller glia.

$$(2)\ dCq = Cq_{\text{reference gene}} - Cq_{\text{gene of interest}}$$

$$(3)\ ddCq = dCq - dCq_{\text{control condition}}$$

$$(4)\ Fold\ change = 2^{\wedge(ddCq)}$$

Retina dissection and fixation

Animals were briefly anesthetized with isoflurane (Zoetis) until breathing slowed, then cervical dislocation was performed. Retinas were immediately dissected from the enucleated eyes in 1X phosphate buffered saline (PBS) and fixed in 4% (w/v) paraformaldehyde for 30 minutes. After 3x PBS washes, retinas were put in 30% (w/v) sucrose in 1X PBS overnight at 4°C for either -80°C freezer storage or immunostaining.

Immunostaining

Staining was carried out in 24-well tissue culture plates (TPP, #92024). Retinas saturated in sucrose (30% sucrose (w/v) in 1X PBS) underwent three freeze/thaw cycles, then were washed 3x with 1X PBS. Next, a blocking step using blocking solution (1% (w/v) bovine serum albumin (Sigma A9418), 5% (v/v) Triton X-100 (Sigma T8787), 0.01% (v/v) sodium

771 azide (VWR 786-299), and 10% (v/v) goat (Millipore S26) or donkey (Millipore S30) serum)
772 was carried out on an orbital shaker for 1 hour at room temperature. Primary antibodies
773 (**Table S2**) were diluted in antibody solution (1% (w/v) bovine serum albumin, 5% (v/v)
774 triton X-100, 0.01% (v/v) sodium azide, 3% (v/v) goat or donkey serum) and incubated for
775 three nights at 4°C on an orbital shaker. Following 3x PBS washes for 30 mins each,
776 secondary solutions were prepared in the antibody solution and incubated at room
777 temperature for 2 hours. After three washes, Hoechst 334422 (1:5,000, Thermo Fisher
778 Scientific, H3570) for 10 mins, and three more 1X PBS washes. Retinas were mounted using
779 an antifade solution (10% (v/v) mowiol (Sigma, 81381), 26% (v/v) glycerol (Sigma, G7757),
780 0.2M tris buffer pH 8, 2.5% (w/v) Dabco (Sigma, D27802)) on glass microscope slides with
781 parafilm spacers to prevent tissue distortion and overlaid with coverslips (VWR, #631-0147).
782
783 *Confocal microscopy*
784 Single cell images for deconvolution were acquired on Zeiss LSM800 microscope using a
785 Plan-Apochromat 40X objective NA 1.4 (#420762-9900) at 1.5x digital zoom to acquire a
786 pixel size of 0.05 µm in X and Y resolution and 0.150 µm in Z. Images were acquired from
787 the peripheral region of the retina, in two opposing quadrants, and inner plexiform layer
788 microglia were selected by setting the z-stack between the ganglion cell and inner nuclear
789 layer Hoechst staining. Microglia in the ganglion cell layer were excluded due to their low
790 population in naïve environment, and known migration from the optic nerve head to the nerve
791 fiber layer after ONC (Heuss et al., 2018). After IPL selection, the IBA1 channel was
792 visualized and the nearest $IBA1^{+}$ cell was selected for imaging, thereby reducing bias in cell
793 selection and blinded to the mitochondrial architecture within the cell. Tile scans (2x2) were
794 necessary to acquire the area of single IPL microglia in naïve condition, resulting in images
795 of dimension 202 x 202 µm. For each animal, 2-3 images for from two opposing quadrants
796 were acquired. Images were stitched using Zen 2.3 or 3.5 desktop version.
797
798 Tiled (2x2) images for C57Bl6/J timecourse ONC experiments (Figure S2) were acquired
799 using a Plan-Apochromat 40X objective NA 1.4 (#420762-9900) with pixel size of 0.156 µm
800 in X and Y and 0.21 µm in Z plane for a region measuring 303 x303 µm. Tiled images (2x2)
801 for microglia and retinal ganglion cell counting were acquired using a Plan-Apochromat 20X
802 objective NA 0.8 (#420650-9901) with pixel resolution 0.312 x 0.312 x 0.5 µm to obtain a
803 region measuring 605 x 605 µm in four peripheral quadrants of each retinal wholemount.
804

805 *Image processing*
806 SVI Huygens Professional v21.10 (https://svi.nl/HomePage) was used for batch
807 deconvolution processing of stitched confocal images. Microscope parameters for batch
808 settings were as follows: 50 nm sampling intervals for X and Y, 150 nm in Z. The refractive
809 index and embedding medium were set to 1.515 and 1.49, respectively. Objective quality was
810 listed as 'good.' For channel settings, the back projected pinhole was set to 250 nm, and the
811 excitation fill factor was 2. Excitation (ex) and emission (em) settings for the four channels
812 were as follows: 405/420 nm, 488/520 nm, 561/602 nm, 633/650 nm. Deconvolution
813 parameters were the default settings for the 'confocal low template' for deconvolution using
814 the classic MLE (maximum likelihood estimation) algorithm with maximum 30 iterations.
815 Images were output in the Imaris file format.
816
817 *Filament tracing*
818 Microglia morphology was traced in 3-dimensions using the *Filament* wizard in IMARIS.
819 The starting point was detected with diameter 12 µm and 0.6 µm was used to set seeding
820 points and the disconnected segment filtering smoothness. Final filament traces were
821 manually edited to remove incorrect segments from the semi-automatic *Filament* tracing.
822 These settings were used for both single cell traces and C57Bl6/J traces from multiple cells in
823 a larger field of view.
824
825 *CD68 volume rendering for multiple cells in field of view*
826 Quantification of CD68 volume per microglia in Figure S2 was performed using Imaris v9.3
827 using the *Surface* wizard. 3d-surface renderings were generated for the CD68 channel using
828 surface detail 0.2 µm and IBA1 channel using 0.5 µm. The *surface-surface coloc* plugin was
829 used to determine the CD68 surfaces within microglia IBA1 surface. The co-localized CD68
830 surfaces total volume was extracted and expressed as a ratio of the total microglia volume.
831 The volumes and ratios were calculated from the entire image.
832
833 *Mitochondria and CD68 surfaces in single microglia*
834 Surface rendering analysis was performed using IMARIS v9.1-9.3 (Bitplane, Imaris).
835 Individual cells were cropped from the original tiled image when necessary to reduce
836 processing time. Then, 3-dimensional surfaces were created for microglia, mitochondria and
837 CD68 vesicles using the *Surface* wizard with surface details settings of 0.5 µm, 0.2 µm, and
838 0.4 µm, respectively. Each surface was manually edited to resolve any inconsistencies in

839 surface creation. Mitochondrial surfaces were carefully edited to verify connectivity
840 throughout the entirety of the network, often requiring manual splitting of surfaces which
841 were joined by the thresholding within the wizard.
842
843 *Mitochondrial organelle and CD68 vesicle localization in single microglia*
844 Completed *Surfaces* for either mitochondria or CD68 were 'split' using the Xtension *Split*
845 *Surfaces* available via Imaris bitplane (https://imaris.oxinst.com/open/). This generates a *Split*
846 *Surface* group where each individual organelle/vesicle becomes a new uniquely named
847 *surface* nested within the *Split Surface* group. A *spot* 5 µm in diameter was manually added
848 to identify the nucleus. Then, the *Spots and Surfaces distance* XTension calculates the
849 distance between the nucleus *spot* and the center point of each individual *surface* in the *Split*
850 *surface* group. The Xtension was modified from the original version to allow for up to 100
851 distance calculations and to output a *csv* file.
852
853 *Data compilation and metric calculations*
854 Python version 3.7 with packages *pandas* (Mckinney, 2010), *matplotlib* (Hunter, 2007) and
855 *seaborn* (Waskom, 2021) for data compilation and visualization. From Imaris, mitochondria,
856 microglia, and CD68 surfaces, microglia filament tracings, and mitochondrial and CD68
857 localization *Statistics* files for each cell were exported to comma separated values file format
858 with a unique identifier for ease in compiling cell-specific data for downstream analysis.
859 Metric calculations for each surface type are detailed below:
860
861 <u>Filament tracing</u>
862 The 'Number of Filament Sholl intersections' from the *Statistics* file was used to plot the
863 number of intersections per increasing radii of 1 µm (Sholl, 1953). Plotted Sholl curves were
864 truncated at 60 µm.
865
866 <u>Median mitochondrial volume and number</u>
867 From the *Statistics* file, the volume of each mitochondrial *Surface* within a cell was used to
868 determine the median mitochondrial volume per cell. Here, the total number of organelles per
869 cell was also be extracted.
870
871 <u>Percentage of CD68 volume</u>

872 From the *Statistics* file, the volume from each CD68 *Surface* within a cell was summed.
873 Additionally, the sum volume of the microglia *Surface* was extracted from the microglia
874 *Statistics* file. The percentage of CD68 volume was calculated from total CD68 volume per
875 total microglia volume for each cell.
876
877 Percentage of mitochondrial volume
878 From the *Statistics* file, the volume from each mitochondrial *Surface* within a cell was
879 summed. Additionally, the sum volume of the microglia *Surface* was extracted from the
880 microglia *Statistics* file. The percentage of mitochondrial volume was calculated from total
881 mitochondria volume per total microglia volume for each cell.
882
883 Mitochondrial perinuclear localization
884 The *Statistics* file for localization data includes the distance of each organelle from the cell
885 soma (µm) and a unique *Surface ID* that is derived from the original mitochondrial *Surface*.
886 From the *Statistics* file of mitochondrial volume, the *Surface ID* can be used to compile
887 distance and volume for each unique organelle within the cell.
888 The percentage of mitochondrial volume in the perinuclear region was determined by
889 calculating the sum of organelle volumes within a 10 µm radius of the cell soma, and
890 dividing by the total mitochondria volume in that cell. The microglia soma ranges from 5-10
891 µm in diameter due to its non-uniform shape, therefore a 10 µm radius from the center of the
892 soma *Spot* in IMARIS includes ~2.5-5 µm of soma, allowing an estimation of mitochondrial
893 localized in the perinuclear space to be at maximum 5-7 µm from the nuclear membrane.
894 We corroborated this perinuclear boundary distance by principal component analysis of the
895 mitochondrial distances. Mitochondrial distances were binned in increments of 10 µm, and
896 the sum volume in each bin was normalized to total mitochondria volume within a cell. PC
897 loadings of the normalized values confirmed that the two bins contributing the most to
898 principal component loadings for distances between 0-10 µm, and 71-80 µm.
899
900 CD68 peripheral localization
901 CD68 localization data was determined in a similar manner, except that the percentage of
902 vesicles outside the perinuclear region were reported as the sum volume of these organelles
903 divided by the total volume of vesicles in the cell. PCA of binned and normalized CD68
904 volumes resulted in greatest PC loadings in the 0-10 µm bin.
905

906 *Identifying Sholl radii for PCA analysis*
907 The Sholl curve (see Method: Filament tracing) is a high-dimensional, vector representation
908 of the microglial morphology. To incorporate filament tracing into the PCA without
909 overpowering the other scalar parameters, we first determined which Sholl radius contributed
910 most to the differences in Sholl intersection curves. Here, Sholl intersections with 10 µm
911 radial distances were normalized for each cell. We observed the greatest PC loadings in the
912 11-20 µm bin. We repeated this analysis with 5 µm radial distances and confirmed the
913 greatest PC loadings in 11-15 µm bin. As the PC loading was greater for the 10 µm radial
914 increments, we implemented the normalized ratio of Sholl intersections at 11-20 µm for each
915 cell and refer to this as the Sholl index.
916
917 *Principal Component Analysis (PCA)*
918 PCA analysis was performed using scikit-learn in Python (Pedregosa et al., 2011). Prior to
919 PCA, a correlation analysis was performed to determine whether any of the individual
920 microglial or mitochondrial metrics derived from the same surface were highly correlated
921 with one another. PCA was then implemented on the metrics or groups of metrics as
922 indicated in Figure legends. In Figure 4, the following seven metrics were used from
923 mitochondria and microglia analysis to serve as components for PCA including; median
924 mitochondria volume, number of mitochondria, percentage of mitochondrial volume per
925 microglia and percentage of CD68 volume per microglia volume were included as mean
926 values for each cell. Mitochondria and CD68 localization values were included as percentage
927 values. Figure 5 used only mitochondrial parameters, while Figure S4 used the Sholl index
928 and CD68 parameters as denoted within the text. In Figure 6, PCA was performed using dCq
929 values of metabolic and stress genes. If a transcript was undetected, a mean Cq value was of
930 40 was used.
931
932 *Cell counting*
933 RBPMS^{+}-cells were counted using the *Spots* function of Imaris v9.3, with additional manual
934 editing. Each of these metrics was quantified from four peripheral quadrants of each analyzed
935 retina and represented as a median value.
936
937 *Statistics*
938 Statistical tests were performed using the Python module *statsmodels* (Seabold and Perktold,
939 2010) as indicated in the figure legends. Groups for comparison were first tested for normal

940 distribution and equal variance using the Shapiro test and Levene test, respectively. Where
941 applicable, post-hoc tests were performed using either Tukey's multiple comparison of means
942 or Dunn's test in Python *statsmodels* 'multicomp'. Significance levels are indicated using the
943 following notation ($^{n.s}$ $p > 0.05$; $^{*}p < 0.05$; $^{**}p < 0.01$; $^{***}p < 0.001$). For Sholl analysis
944 comparisons, linear regression models from *lme4* package (Bates et al., 2015) were
945 performed in R. The default contrast for unordered variables was changed to 'contr.sum',
946 allowing type III Anova comparison. Statistical analysis for all figure panels are found in
947 **Table S3.**
948
949
950 **References**
951

952 Al-Mehdi, A.B., Pastukh, V.M., Swiger, B.M., Reed, D.J., Patel, M.R., Bardwell, G.C.,
953 Pastukh, V. V., Alexeyev, M.F., and Gillespie, M.N. (2012). Perinuclear mitochondrial
954 clustering creates an oxidant-rich nuclear domain required for hypoxia-induced transcription.
955 Sci. Signal. *5*.
956 Arsenijevic, D., Onuma, H., Pecqueur, C., Raimbault, S., Manning, B.S., Miroux, B.,
957 Couplan, E., Alves-Guerra, M.-C., Goubern, M., Surwit, R., et al. (2000). Disruption of the
958 uncoupling protein-2 gene in mice reveals a role in immunity and reactive oxygen species
959 production. Nat. Genet. *26*, 435–439.
960 Baik, S.H., Kang, S., Lee, W., Choi, H., Chung, S., Kim, J. Il, and Mook-Jung, I. (2019). A
961 Breakdown in Metabolic Reprogramming Causes Microglia Dysfunction in Alzheimer's
962 Disease. Cell Metab. *30*, 493-507.e6.
963 Baker, A.E., Brautigam, V.M., and Watters, J.J. (2004). Estrogen Modulates Microglial
964 Inflammatory Mediator Production via Interactions with Estrogen Receptor β. Endocrinology
965 *145*, 5021–5032.
966 Bates, D., Mächler, M., Bolker, B.M., and Walker, S.C. (2015). Fitting Linear Mixed-Effects
967 Models Using lme4. J. Stat. Softw. *67*, 1–48.
968 Bauer, J., Sminia, T., Wouterlood, F.G., and Dijkstra, C.D. (1994). Phagocytic activity of
969 macrophages and microglial cells during the course of acute and chronic relapsing
970 experimental autoimmune encephalomyelitis. J. Neurosci. Res. *38*, 365–375.
971 Bernier, L.P., York, E.M., and MacVicar, B.A. (2020). Immunometabolism in the Brain:
972 How Metabolism Shapes Microglial Function. Trends Neurosci. *43*, 854–869.
973 Borst, K., Schwabenland, M., and Prinz, M. (2019). Microglia metabolism in health and

974 disease. Neurochem. Int. *130*, 104331.
975 Bronstein, R., Torres, L., Nissen, J.C., and Tsirka, S.E. (2013). Culturing microglia from the
976 neonatal and adult central nervous system. J. Vis. Exp.
977 Buck, M.D., O'Sullivan, D., Klein Geltink, R.I., Curtis, J.D., Chang, C.-H., Sanin, D.E., Qiu,
978 J., Kretz, O., Braas, D., van der Windt, G.J.W., et al. (2016). Mitochondrial Dynamics
979 Controls T Cell Fate through Metabolic Programming. Cell *166*, 63–76.
980 Colombo, G., Cubero, R.J.A., Kanari, L., Venturino, A., Schulz, R., Scolamiero, M.,
981 Agerberg, J., Mathys, H., Tsai, L.-H., Chachólski, W., et al. (2021). Microglial MorphOMICs
982 unravel region- and sex-dependent morphological phenotypes from postnatal development to
983 degeneration. BioRxiv 2021.11.30.470610.
984 Damoiseaux, J.G., Döpp, E.A., Calame, W., Chao, D., MacPherson, G.G., and Dijkstra, C.D.
985 (1994). Rat macrophage lysosomal membrane antigen recognized by monoclonal antibody
986 ED1. Immunology *83*, 140–147.
987 Das, R., and Chakrabarti, O. (2020). Mitochondrial hyperfusion: a friend or a foe. Biochem.
988 Soc. Trans. *48*, 631–644.
989 Erny, D., Dokalis, N., Mezö, C., Castoldi, A., Mossad, O., Staszewski, O., Frosch, M., Villa,
990 M., Fuchs, V., Mayer, A., et al. (2021). Microbiota-derived acetate enables the metabolic
991 fitness of the brain innate immune system during health and disease. Cell Metab. *33*, 2260-
992 2276.e7.
993 Faas, M., Ipseiz, N., Ackermann, J., Culemann, S., Grüneboom, A., Schröder, F., Rothe, T.,
994 Scholtysek, C., Eberhardt, M., Böttcher, M., et al. (2021). IL-33-induced metabolic
995 reprogramming controls the differentiation of alternatively activated macrophages and the
996 resolution of inflammation. Immunity.
997 Finck, B.N., and Kelly, D.P. (2006). PGC-1 coactivators: inducible regulators of energy
998 metabolism in health and disease. J. Clin. Invest. *116*, 615.
999 Galatro, T.F., Holtman, I.R., Lerario, A.M., Vainchtein, I.D., Brouwer, N., Sola, P.R., Veras,
1000 M.M., Pereira, T.F., Leite, R.E.P., M?ller, T., et al. (2017). Transcriptomic analysis of
1001 purified human cortical microglia reveals age-associated changes. Nat. Neurosci.
1002 Galindo-Romero, C., Valiente-Soriano, F.J., Jiménez-López, M., García-Ayuso, D., Villegas-
1003 Pérez, M.P., Vidal-Sanz, M., and Agudo-Barriuso, M. (2013). Effect of Brain-Derived
1004 Neurotrophic Factor on Mouse Axotomized Retinal Ganglion Cells and Phagocytic
1005 Microglia. Invest. Ophthalmol. Vis. Sci. *54*, 974–985.
1006 Goldmann, T., Wieghofer, P., Müller, P.F., Wolf, Y., Varol, D., Yona, S., Brendecke, S.M.,
1007 Kierdorf, K., Staszewski, O., Datta, M., et al. (2013). A new type of microglia gene targeting

1008 shows TAK1 to be pivotal in CNS autoimmune inflammation. Nat. Neurosci. 2013 1611 *16*,
1009 1618–1626.
1010 Gomes, L.C., Benedetto, G. Di, and Scorrano, L. (2011). During autophagy mitochondria
1011 elongate, are spared from degradation and sustain cell viability. Nat. Cell Biol. 2011 135 *13*,
1012 589–598.
1013 Gosselin, D., Skola, D., Coufal, N.G., Holtman, I.R., Schlachetzki, J.C.M.M., Sajti, E.,
1014 Jaeger, B.N., O'Connor, C., Fitzpatrick, C., Pasillas, M.P., et al. (2017). An environment-
1015 dependent transcriptional network specifies human microglia identity. Science (80-.). *356*,
1016 1248–1259.
1017 Hammond, T.R., Dufort, C., Dissing-Olesen, L., Giera, S., Young, A., Wysoker, A., Walker,
1018 A.J., Gergits, F., Segel, M., Nemesh, J., et al. (2019). Single-Cell RNA Sequencing of
1019 Microglia throughout the Mouse Lifespan and in the Injured Brain Reveals Complex Cell-
1020 State Changes. Immunity.
1021 Hanisch, U.-K., and Kettenmann, H. (2007). Microglia: active sensor and versatile effector
1022 cells in the normal and pathologic brain. Nat. Neurosci. *10*, 1387–1394.
1023 He, D., Xu, H., Zhang, H., Tang, R., Lan, Y., Xing, R., Li, S., Christian, E., Hou, Y., Lorello,
1024 P., et al. (2022). Disruption of the IL-33-ST2-AKT signaling axis impairs neurodevelopment
1025 by inhibiting microglial metabolic adaptation and phagocytic function. Immunity *55*, 159-
1026 173.e9.
1027 Heuss, N.D., Pierson, M.J., Roehrich, H., McPherson, S.W., Gram, A.L., Li, L., and
1028 Gregerson, D.S. (2018). Optic nerve as a source of activated retinal microglia post-injury.
1029 Acta Neuropathol. Commun. *6*, 66.
1030 Hilla, A.M., Diekmann, H., and Fischer, D. (2017). Microglia Are Irrelevant for Neuronal
1031 Degeneration and Axon Regeneration after Acute Injury. J. Neurosci. *37*, 6113–6124.
1032 Hoang, T., Wang, J., Boyd, P., Wang, F., Santiago, C., Jiang, L., Yoo, S., Lahne, M., Todd,
1033 L.J., Jia, M., et al. (2020). Gene regulatory networks controlling vertebrate retinal
1034 regeneration. Science (80-.). *934*, eabb8598.
1035 Horimoto, M., Resnick, M.B., Konkin, T.A., Routhier, J., Wands, J.R., and Baffy, G. (2004).
1036 Expression of uncoupling protein-2 in human colon cancer. Clin. Cancer Res. *10*, 6203–6207.
1037 Van Hove, H., Antunes, A.R.P., De Vlaminck, K., Scheyltjens, I., Van Ginderachter, J.A.,
1038 and Movahedi, K. (2020). Identifying the variables that drive tamoxifen-independent
1039 CreERT2 recombination: Implications for microglial fate mapping and gene deletions. Eur. J.
1040 Immunol. *50*, 459–463.
1041 Hunter, J.D. (2007). Matplotlib: A 2D graphics environment. Comput. Sci. Eng. *9*, 90–95.

1042 Jahn, H.M., Kasakow, C. V., Helfer, A., Michely, J., Verkhratsky, A., Maurer, H.H.,
1043 Scheller, A., and Kirchhoff, F. (2018). Refined protocols of tamoxifen injection for inducible
1044 DNA recombination in mouse astroglia. Sci. Reports 2018 81 *8*, 1–11.
1045 Ježek, P., Holendová, B., Garlid, K.D., and Jabůrek, M. (2018). Mitochondrial Uncoupling
1046 Proteins: Subtle Regulators of Cellular Redox Signaling. Antioxid. Redox Signal. *29*, 667–
1047 714.
1048 Jha, A.K., Huang, S.C.C., Sergushichev, A., Lampropoulou, V., Ivanova, Y., Loginicheva,
1049 E., Chmielewski, K., Stewart, K.M., Ashall, J., Everts, B., et al. (2015). Network integration
1050 of parallel metabolic and transcriptional data reveals metabolic modules that regulate
1051 macrophage polarization. Immunity *42*, 419–430.
1052 Kim, J.D., Yoon, N.A., Jin, S., and Diano, S. (2019). Microglial UCP2 Mediates
1053 Inflammation and Obesity Induced by High-Fat Feeding. Cell Metab. *30*, 952-962.e5.
1054 Kong, D., Vong, L., Parton, L.E., Ye, C., Tong, Q., Hu, X., Choi, B., Brüning, J.C., and
1055 Lowell, B.B. (2010). Glucose Stimulation of Hypothalamic MCH Neurons Involves KATP
1056 Channels, Is Modulated by UCP2, and Regulates Peripheral Glucose Homeostasis. Cell
1057 Metab. *12*, 545–552.
1058 Levkovitch-Verbin, H., Harris-Cerruti, C., Groner, Y., Wheeler, L.A., Schwartz, M., and
1059 Yoles, E. (2000). RGC death in mice after optic nerve crush injury: Oxidative stress and
1060 neuroprotection. Investig. Ophthalmol. Vis. Sci. *41*, 4169–4174.
1061 Li, Y., Schlamp, C.L., and Nickells, R.W. (1999). Experimental induction of retinal ganglion
1062 cell death in adult mice. Invest. Ophthalmol. Vis. Sci. *40*, 1004–1008.
1063 Libby, R.T., Anderson, M.G., Pang, I.H., Robinson, Z.H., Savinova, O. V., Cosma, I.M.,
1064 Snow, A., Wilson, L.A., Smith, R.S., Clark, A.F., et al. (2005). Inherited glaucoma in
1065 DBA/2J mice: Pertinent disease features for studying the neurodegeneration. Vis. Neurosci.
1066 *22*, 637–648.
1067 Liu, S., Li, Z.W., Weinreb, R.N., Xu, G., Lindsey, J.D., Ye, C., Yung, W.H., Pang, C.P.,
1068 Lam, D.S.C., and Leung, C.K.S. (2012). Tracking retinal microgliosis in models of retinal
1069 ganglion cell damage. Investig. Ophthalmol. Vis. Sci. *53*, 6254–6262.
1070 Maes, M.E., Schlamp, C.L., and Nickells, R.W. (2017). BAX to basics: How the BCL2 gene
1071 family controls the death of retinal ganglion cells. Prog. Retin. Eye Res. *57*, 1–25.
1072 Man, P.Y.W., Griffiths, P.G., Brown, D.T., Howell, N., Turnbull, D.M., and Chinnery, P.F.
1073 (2003). The Epidemiology of Leber Hereditary Optic Neuropathy in the North East of
1074 England. Am. J. Hum. Genet. *72*, 333–339.
1075 Masuda, T., Sankowski, R., Staszewski, O., and Prinz, M. (2020). Microglia Heterogeneity in

1076 the Single-Cell Era. CellReports *30*, 1271–1281.
1077 Matcovitch-Natan, O., Winter, D.R., Giladi, A., Vargas Aguilar, S., Spinrad, A., Sarrazin, S.,
1078 Ben-Yehuda, H., David, E., Zelada González, F., Perrin, P., et al. (2016). Microglia
1079 development follows a stepwise program to regulate brain homeostasis. Science *353*,
1080 aad8670.
1081 Mckinney, W. (2010). Data Structures for Statistical Computing in Python.
1082 Mishra, P., and Chan, D.C. (2016). Metabolic regulation of mitochondrial dynamics. J. Cell
1083 Biol. *212*, 379–387.
1084 Mitra, K., Wunder, C., Roysam, B., Lin, G., and Lippincott-Schwartz, J. (2009). A
1085 hyperfused mitochondrial state achieved at G1-S regulates cyclin E buildup and entry into S
1086 phase. Proc. Natl. Acad. Sci. U. S. A. *106*, 11960–11965.
1087 Nair, S., Sobotka, K.S., Joshi, P., Gressens, P., Fleiss, B., Thornton, C., Mallard, C., and
1088 Hagberg, H. (2019). Lipopolysaccharide-induced alteration of mitochondrial morphology
1089 induces a metabolic shift in microglia modulating the inflammatory response in vitro and in
1090 vivo. Glia *67*, 1047–1061.
1091 Mac Nair, C.E., Schlamp, C.L., Montgomery, A.D., Shestopalov, V.I., and Nickells, R.W.
1092 (2016). Retinal glial responses to optic nerve crush are attenuated in Bax-deficient mice and
1093 modulated by purinergic signaling pathways. J. Neuroinflammation *13*, 93.
1094 Nakazawa, T., Takahashi, H., and Shimura, M. (2006). Estrogen has a neuroprotective effect
1095 on axotomized RGCs through ERK signal transduction pathway. Brain Res. *1093*, 141–149.
1096 Nuzzi, R., and Caselgrandi, P. (2022). Sex Hormones and Their Effects on Ocular Disorders
1097 and Pathophysiology: Current Aspects and Our Experience. Int. J. Mol. Sci. *23*.
1098 O'Koren, E.G., Yu, C., Klingeborn, M., Wong, A.Y.W., Prigge, C.L., Mathew, R., Kalnitsky,
1099 J., Msallam, R.A., Silvin, A., Kay, J.N., et al. (2019). Microglial Function Is Distinct in
1100 Different Anatomical Locations during Retinal Homeostasis and Degeneration. Immunity *50*,
1101 723-737.e7.
1102 Paolicelli, R., Sierra, A., Stevens, B., Tremblay, M.-E., Aguzzi, A., Ajami, B., Amit, I.,
1103 Audinat, E., Bechmann, I., Bennett, M., et al. (2022). Defining Microglial States and
1104 Nomenclature: A Roadmap to 2030. SSRN Electron. J.
1105 Park, J., Choi, H., Min, J.-S., Park, S.-J., Kim, J.-H., Park, H.-J., Kim, B., Chae, J.-I., Yim,
1106 M., and Lee, D.-S. (2013). Mitochondrial dynamics modulate the expression of pro-
1107 inflammatory mediators in microglial cells. J. Neurochem. *127*, 221–232.
1108 Pecqueur, C., Alves-Guerra, M.-C., Gelly, C., Lévi-Meyrueis, C., Couplan, E., Collins, S.,
1109 Ricquier, D., Bouillaud, F., and Miroux, B. (2001). Uncoupling Protein 2, *in Vivo*

1110 Distribution, Induction upon Oxidative Stress, and Evidence for Translational Regulation. J.
1111 Biol. Chem. *276*, 8705–8712.
1112 Pedregosa, F., Varoquaux, G., Gramfort, A., Michel, V., Thirion, B., Grisel, O., Blondel, M.,
1113 Prettenhofer, P., Weiss, R., Dubourg, V., et al. (2011). Scikit-learn: Machine Learning in
1114 Python. J. Mach. Learn. Res. *12*, 2825–2830.
1115 Pham, A.H., McCaffery, J.M., and Chan, D.C. (2012). Mouse lines with photo-activatable
1116 mitochondria to study mitochondrial dynamics. Genesis *50*, 833–843.
1117 Quigley, H., and Broman, A.T. (2006). The number of people with glaucoma worldwide in
1118 2010 and 2020. Br. J. Ophthalmol. *90*, 262–267.
1119 Rambold, A.S., and Pearce, E.L. (2018). Mitochondrial Dynamics at the Interface of Immune
1120 Cell Metabolism and Function. Trends Immunol. *39*, 6–18.
1121 Rodriguez, A.R., de Sevilla Müller, L.P., and Brecha, N.C. (2014). The RNA binding protein
1122 RBPMS is a selective marker of ganglion cells in the mammalian retina. J. Comp. Neurol.
1123 *522*, 1411–1443.
1124 Ron-Harel, N., Santos, D., Ghergurovich, J.M., Sage, P.T., Reddy, A., Lovitch, S.B.,
1125 Dephoure, N., Satterstrom, F.K., Sheffer, M., Spinelli, J.B., et al. (2016). Mitochondrial
1126 biogenesis and proteome remodeling promotes one carbon metabolism for T cell activation.
1127 Cell Metab. *24*, 104.
1128 Rupprecht, A., Bräuer, A.U., Smorodchenko, A., Goyn, J., Hilse, K.E., Shabalina, I.G.,
1129 Infante-Duarte, C., and Pohl, E.E. (2012). Quantification of Uncoupling Protein 2 Reveals Its
1130 Main Expression in Immune Cells and Selective Up-Regulation during T-Cell Proliferation.
1131 PLoS One *7*, e41406.
1132 Rupprecht, A., Sittner, D., Smorodchenko, A., Hilse, K.E., Goyn, J., Moldzio, R., Seiler,
1133 A.E.M., Bräuer, A.U., and Pohl, E.E. (2014). Uncoupling Protein 2 and 4 Expression Pattern
1134 during Stem Cell Differentiation Provides New Insight into Their Putative Function. PLoS
1135 One *9*, e88474.
1136 Rupprecht, A., Moldzio, R., Mödl, B., and Pohl, E.E. (2019). Glutamine regulates
1137 mitochondrial uncoupling protein 2 to promote glutaminolysis in neuroblastoma cells.
1138 Biochim. Biophys. Acta. Bioenerg. *1860*, 391–401.
1139 Salter, M.W., and Stevens, B. (2017). Microglia emerge as central players in brain disease.
1140 Nat. Med. *23*, 1018–1027.
1141 Schmittgen, T.D., and Livak, K.J. (2008). Analyzing real-time PCR data by the comparative
1142 CT method. Nat. Protoc. 2008 36 *3*, 1101–1108.
1143 Seabold, S., and Perktold, J. (2010). Statsmodels: Econometric and Statistical Modeling with

Python. Proc. 9th Python Sci. Conf.

Sholl, D.A. (1953). Dendritic organization in the neurons of the visual and motor cortices of the cat. *87*.

Siegert, S., Cabuy, E., Scherf, B.G., Kohler, H., Panda, S., Le, Y.Z., Fehling, H.J., Gaidatzis, D., Stadler, M.B., and Roska, B. (2012). Transcriptional code and disease map for adult retinal cell types. Nat. Neurosci. *15*, 487–495.

Smorodchenko, A., Schneider, S., Rupprecht, A., Hilse, K., Sasgary, S., Zeitz, U., Erben, R.G., and Pohl, E.E. (2017). UCP2 up-regulation within the course of autoimmune encephalomyelitis correlates with T-lymphocyte activation. Biochim. Biophys. Acta. Mol. Basis Dis. *1863*, 1002–1012.

Spanier, G., Xu, H., Xia, N., Tobias, S., Deng, S., Wojnowski, L., Forstermann, U., and Li, H. (2009). Resveratrol reduces endothelial oxidative stress by modulating the gene expression of superoxide dismutase 1 (SOD1), glutathione peroxidase 1 (GPx1) and NADPH oxidase subunit (Nox4). J. Physiol. Pharmacol. *60 Suppl 4*, 111–116.

Stogsdill, J.A., Kim, K., Binan, L., Farhi, S.L., Levin, J.Z., and Arlotta, P. (2022). Pyramidal neuron subtype diversity governs microglia states in the neocortex. Nat. 2022 1–7.

Thion, M.S., Low, D., Silvin, A., Chen, J., Grisel, P., Schulte-Schrepping, J., Blecher, R., Ulas, T., Squarzoni, P., Hoeffel, G., et al. (2018). Microbiome Influences Prenatal and Adult Microglia in a Sex-Specific Manner. Cell *172*, 500-516.e16.

Toda, C., Kim, J.D., Impellizzeri, D., Cuzzocrea, S., Liu, Z.-W., and Diano, S. (2016). UCP2 Regulates Mitochondrial Fission and Ventromedial Nucleus Control of Glucose Responsiveness. Cell *164*, 872–883.

Tondera, D., Grandemange, S., Jourdain, A., Karbowski, M., Mattenberger, Y., Herzig, S., Da Cruz, S., Clerc, P., Raschke, I., Merkwirth, C., et al. (2009). SLP-2 is required for stress-induced mitochondrial hyperfusion. EMBO J. *28*, 1589–1600.

Ulland, T.K., Song, W.M., Huang, S.C.-C., Ulrich, J.D., Sergushichev, A., Beatty, W.L., Loboda, A.A., Zhou, Y., Cairns, N.J., Kambal, A., et al. (2017). TREM2 Maintains Microglial Metabolic Fitness in Alzheimer's Disease. Cell *170*, 649-663.e13.

Villa, A., Gelosa, P., Castiglioni, L., Cimino, M., Rizzi, N., Pepe, G., Lolli, F., Marcello, E., Sironi, L., Vegeto, E., et al. (2018). Sex-Specific Features of Microglia from Adult Mice. Cell Rep. *23*, 3501–3511.

Vozza, A., Parisi, G., Leonardis, F. De, Lasorsa, F.M., and Castegna, A. (2014). UCP2 transports C4 metabolites out of mitochondria, regulating glucose and glutamine oxidation. *111*, 960–965.

Wai, T., and Langer, T. (2016). Mitochondrial Dynamics and Metabolic Regulation. Trends Endocrinol. Metab. *27*, 105–117.

Waskom, M.L. (2021). seaborn: statistical data visualization. J. Open Source Softw. *6*, 3021.

Williams, P.R., Benowitz, L.I., Goldberg, J.L., and He, Z. (2020). Axon Regeneration in the Mammalian Optic Nerve. Annu. Rev. Vis. Sci. *6*, 195–213.

Wohl, S.G., Schmeer, C.W., Witte, O.W., and Isenmann, S. (2010). Proliferative response of microglia and macrophages in the adult mouse eye after optic nerve lesion. Investig. Ophthalmol. Vis. Sci. *51*, 2686–2696.

Yang, S.-H., Liu, R., Perez, E.J., Wen, Y., Stevens, S.M.†, Valencia, T., Brun-Zinkernagel, A.-M., Prokai, L., Will, Y., Dykens, J., et al. (2004). Mitochondrial localization of estrogen receptor.

Yasumoto, Y., Stoiljkovic, M., Kim, J.D., Sestan-Pesa, M., Gao, X.-B., Diano, S., and Horvath, T.L. (2021). Ucp2-dependent microglia-neuronal coupling controls ventral hippocampal circuit function and anxiety-like behavior. Mol. Psychiatry 2021 1–13.

Yona, S., Kim, K.-W., Wolf, Y., Mildner, A., Varol, D., Breker, M., Strauss-Ayali, D., Viukov, S., Guilliams, M., Misharin, A., et al. (2013). Fate Mapping Reveals Origins and Dynamics of Monocytes and Tissue Macrophages under Homeostasis. Immunity *38*, 79–91.

Youle, R.J., and van der Bliek, A.M. (2012). Mitochondrial Fission, Fusion, and Stress. Science (80-.). *337*, 1062–1065.

Zhang, J., Khvorostov, I., Hong, J.S., Oktay, Y., Vergnes, L., Nuebel, E., Wahjudi, P.N., Setoguchi, K., Wang, G., Do, A., et al. (2011). UCP2 regulates energy metabolism and differentiation potential of human pluripotent stem cells. EMBO J. *30*, 4860–4873.

Žuna, K., Jovanović, O., Khailova, L.S., Škulj, S., Brkljača, Z., Kreiter, J., Kotova, E.A., Vazdar, M., Antonenko, Y.N., and Pohl, E.E. (2021). Mitochondrial uncoupling proteins (UCP1-UCP3) and adenine nucleotide translocase (ANT1) enhance the protonophoric action of 2,4-dinitrophenol in mitochondria and planar bilayer membranes. Biomolecules *11*.

Figure 1.

A

Mouse model for mitochondrial visualization

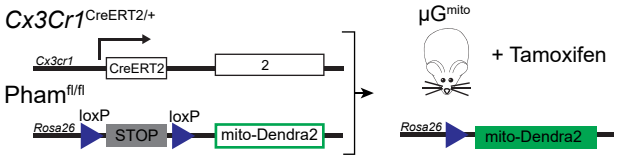

D

Mouse model for mitochondrial visualization and manipulation

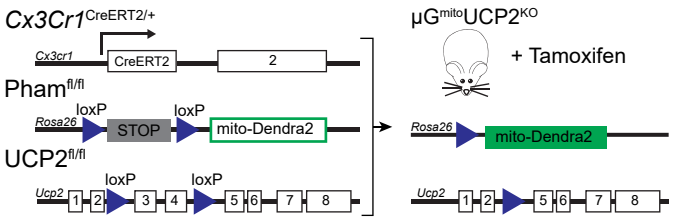

B

Microglia-specific mitochondrial label in μG^{mito}

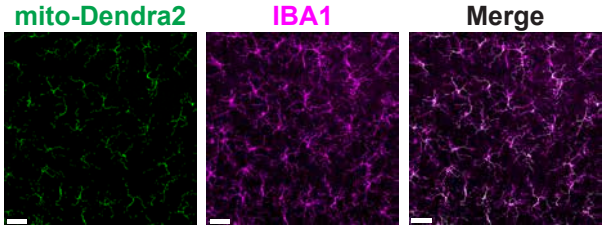

E

Microglia-specific mitochondria label in μG^{mito}UCP2^{KO}

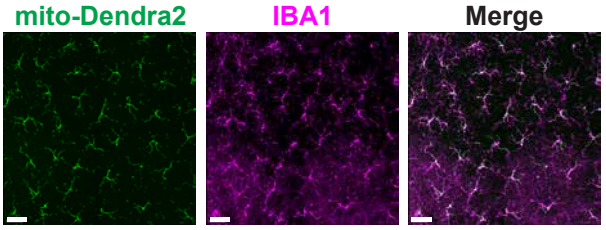

C

μG^{mito} single-cell mitochondrial analysis

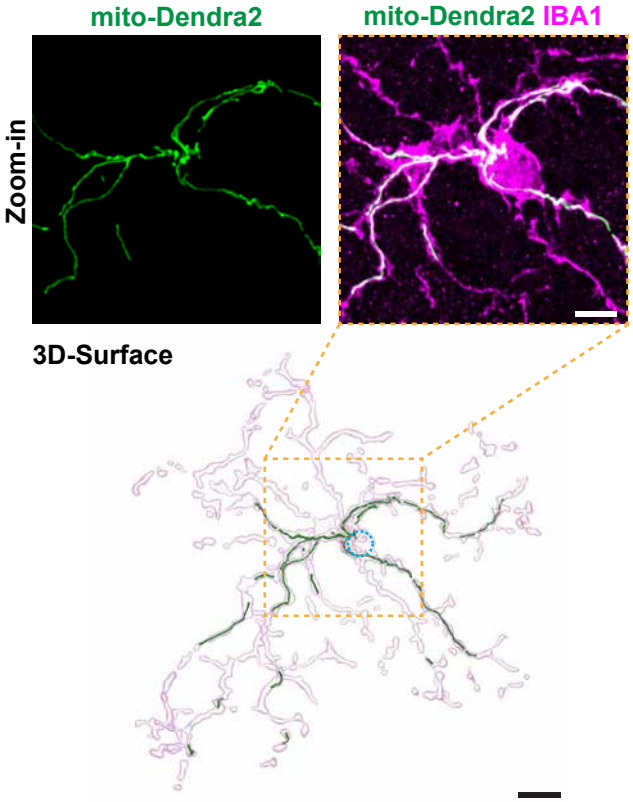

F

μG^{mito}UCP2^{KO} single-cell mitochondrial analysis

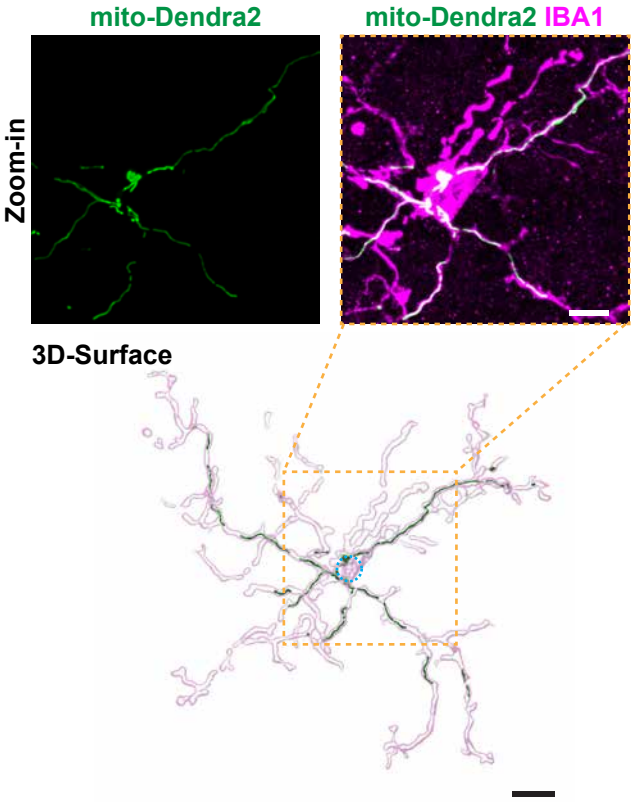

G

Mitochondrial network connectivity

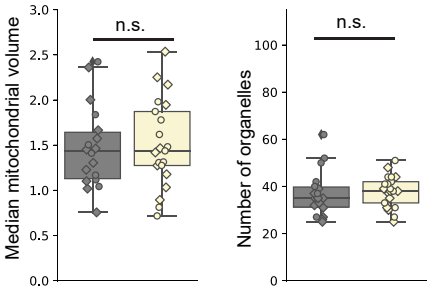

H

Mitochondrial content

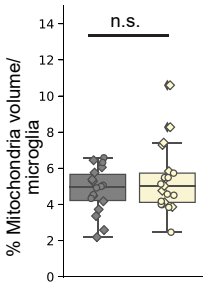

I

Mitochondrial localization

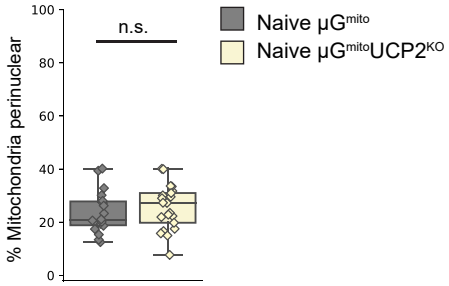

Figure 2.

A *Optic nerve crush (ONC)*

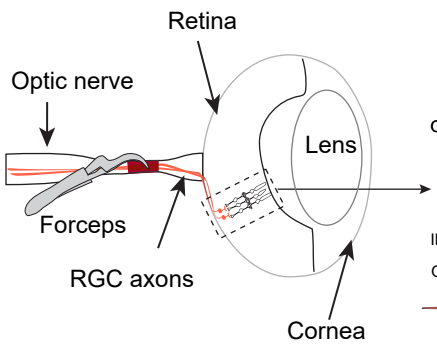

B *ONC elicits IPL microglia response 5 days post-injury*

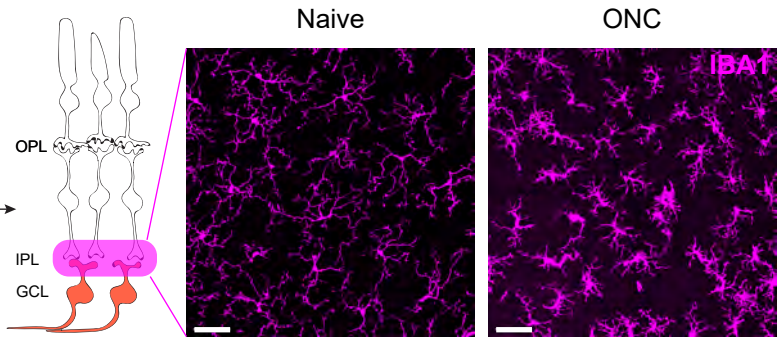

C *Microglial Ucp2 transcript increases upon ONC*

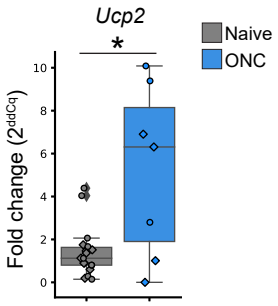

μG^mito Naive | **μG^mito ONC** | **Analysis**

3D-trace

D

G

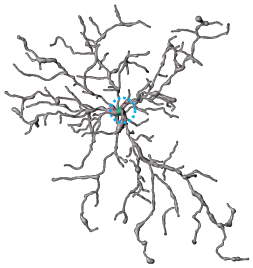

J *Sholl intersections*

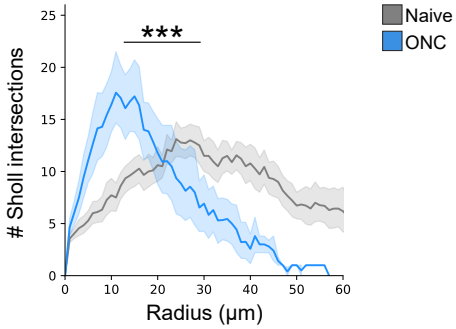

CD68 surface

E

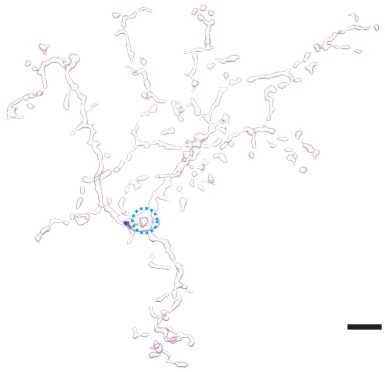

H

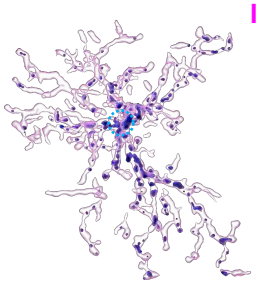

K *CD68 volume*

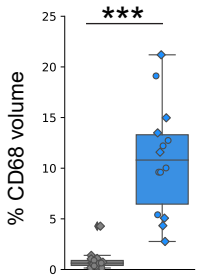

L *CD68 localization*

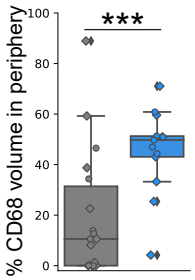

Mitochondria surface

F

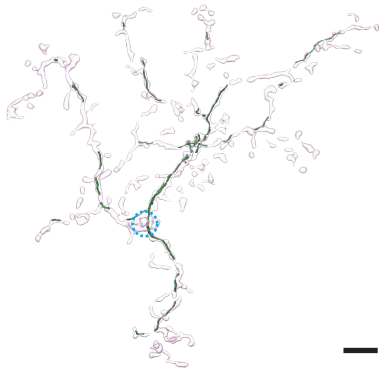

I

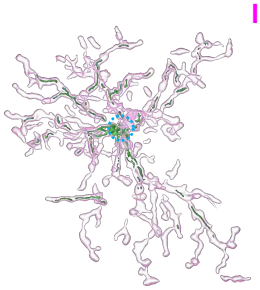

M *Mitochondrial network connectivity*

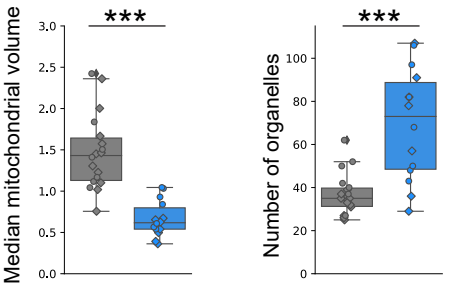

N *Mitochondrial content*

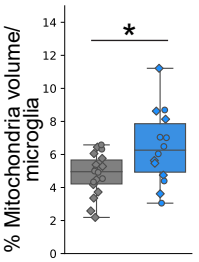

O *Mitochondrial localization*

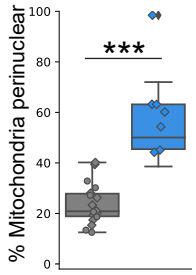

Figure 3.

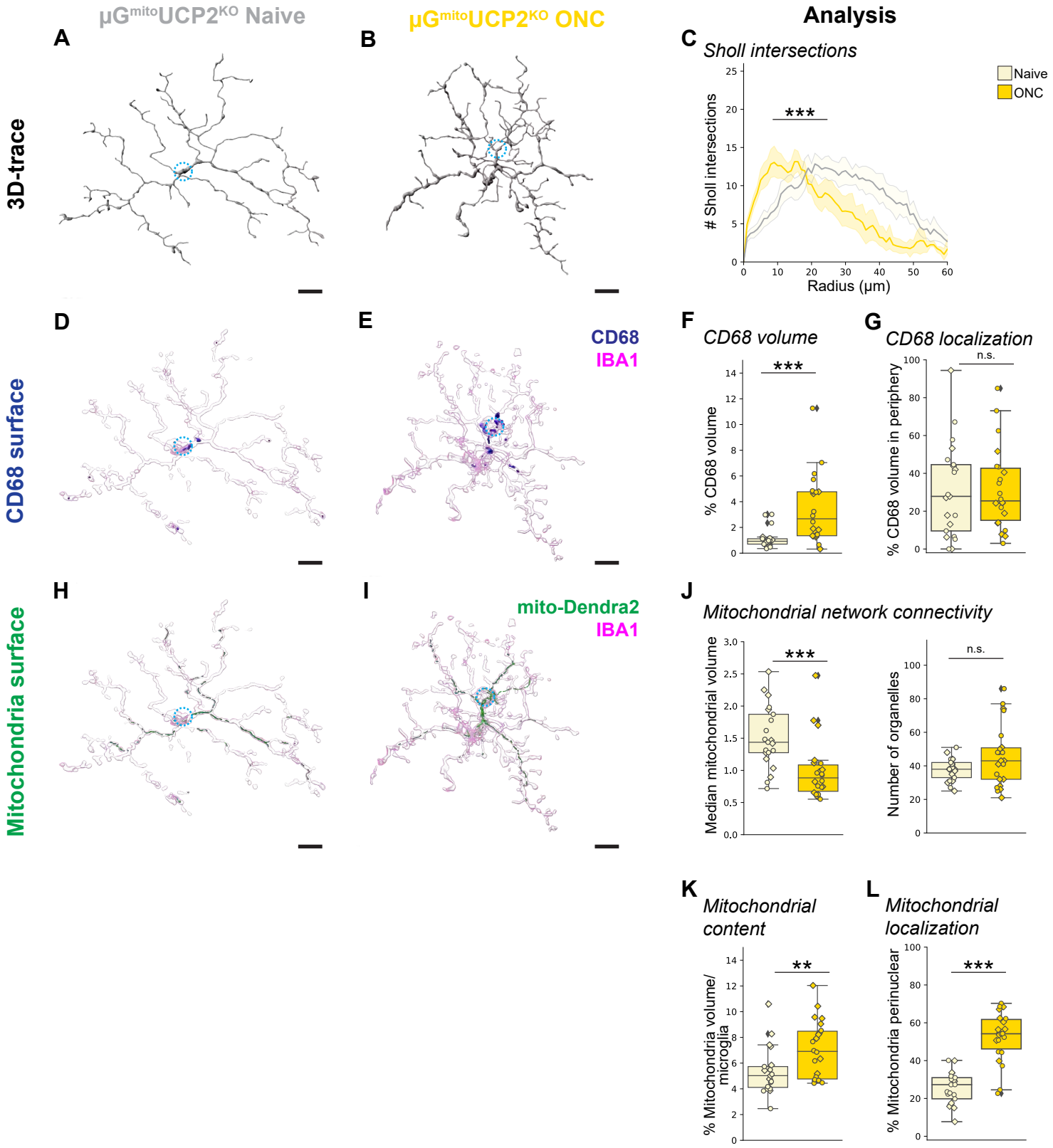
μG^mitoUCP2^KO Naive
μG^mitoUCP2^KO ONC
Analysis
A
B
C
Sholl intersections
Naive
ONC
***
Sholl intersections
Radius (μm)
3D-trace
D
E
CD68
IBA1
F
CD68 volume
***
% CD68 volume
G
CD68 localization
n.s.
% CD68 volume in periphery
CD68 surface
H
I
mito-Dendra2
IBA1
J
Mitochondrial network connectivity
***
Median mitochondrial volume
n.s.
Number of organelles
Mitochondria surface
K
Mitochondrial content
**
% Mitochondria volume/ microglia
L
Mitochondrial localization
***
% Mitochondria perinuclear

Figure 4.

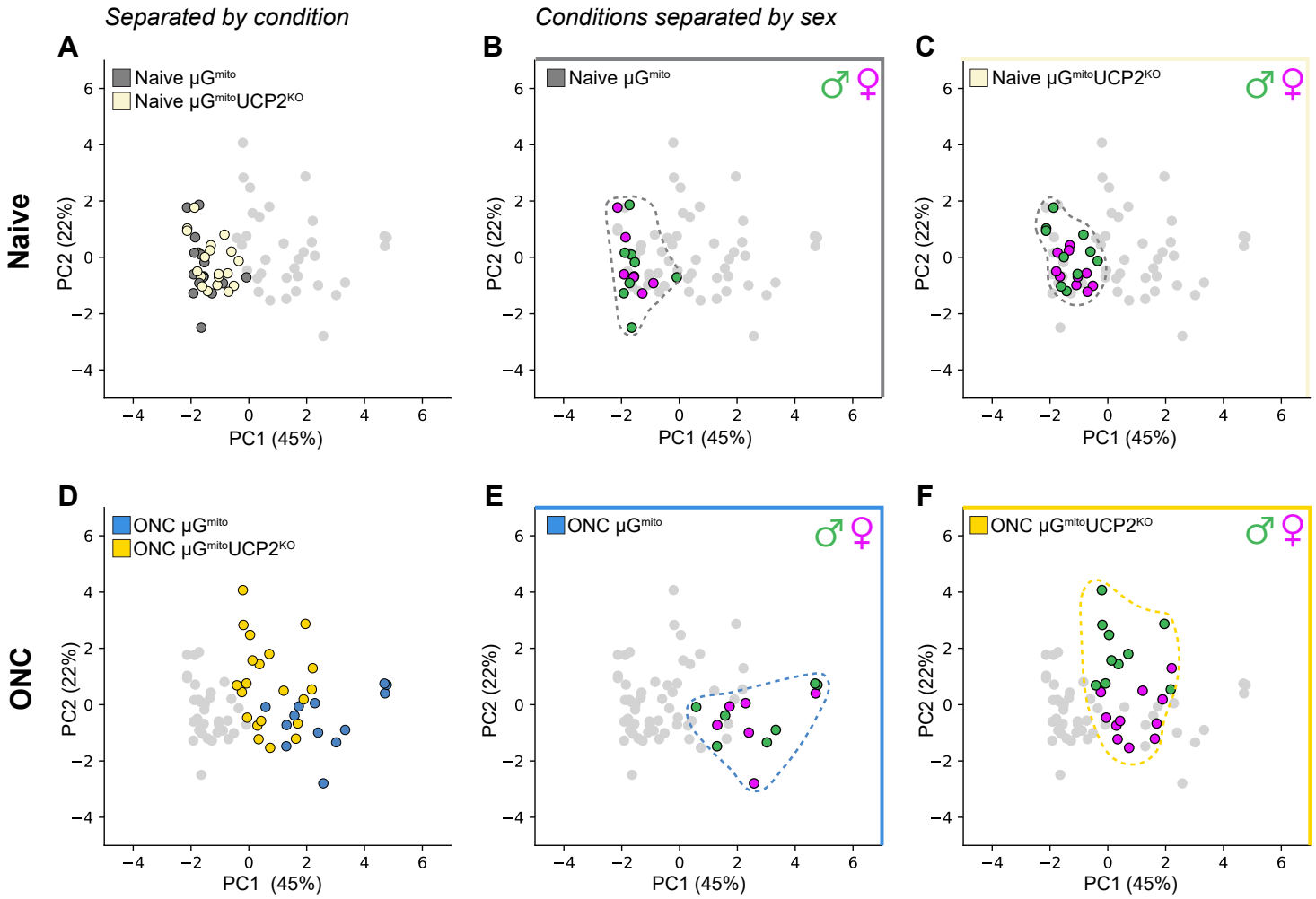
Separated by condition
Conditions separated by sex
A
B
C
D
E
F
Naive
ONC
Naive μG^mito
Naive μG^mito UCP2^KO
ONC μG^mito
ONC μG^mito UCP2^KO
♂ ♀
PC1 (45%)
PC2 (22%)

Figure 5.

Mitochondrial parameter PCA

Separated by condition

Conditions separated by sex

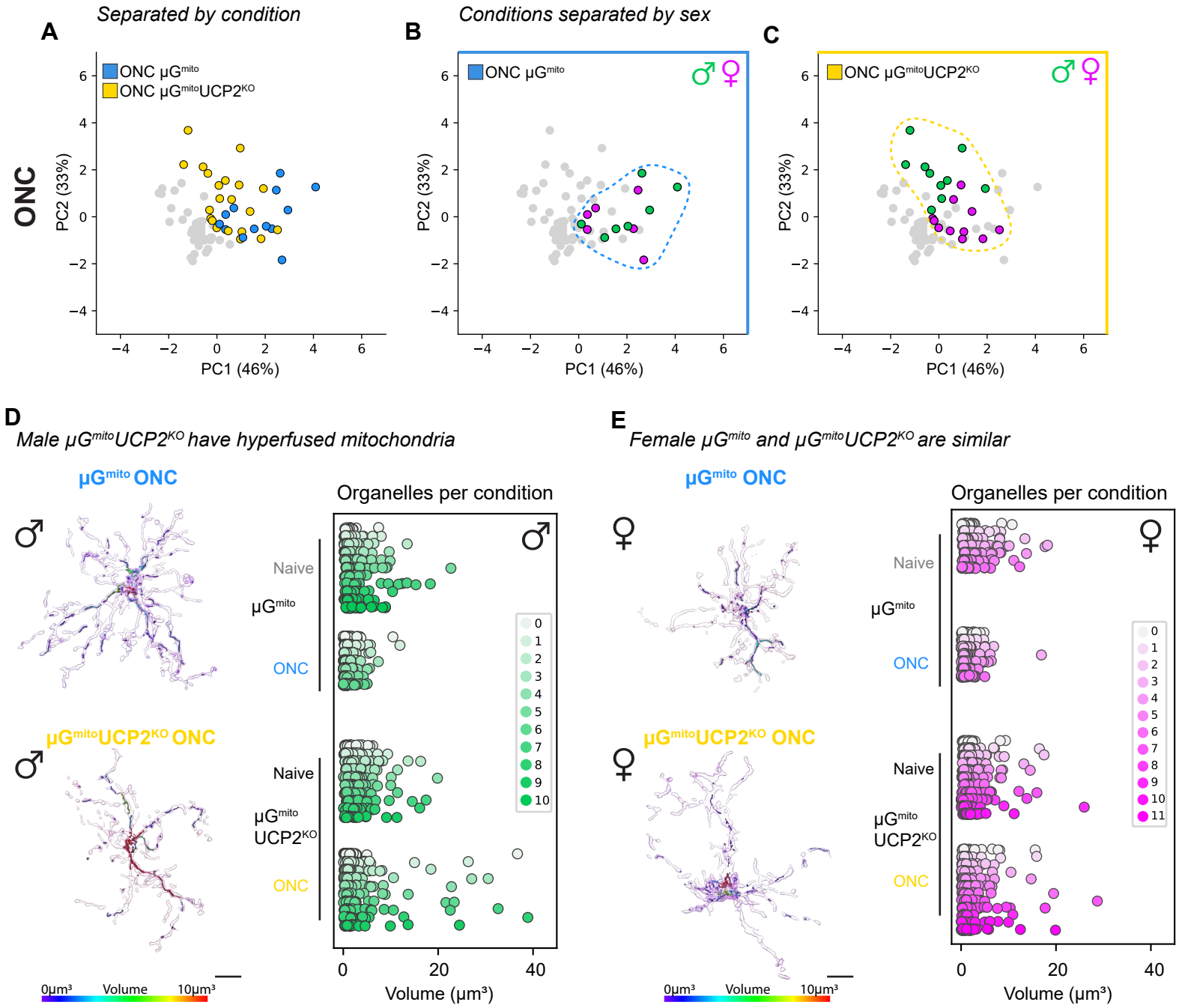

Figure 6.

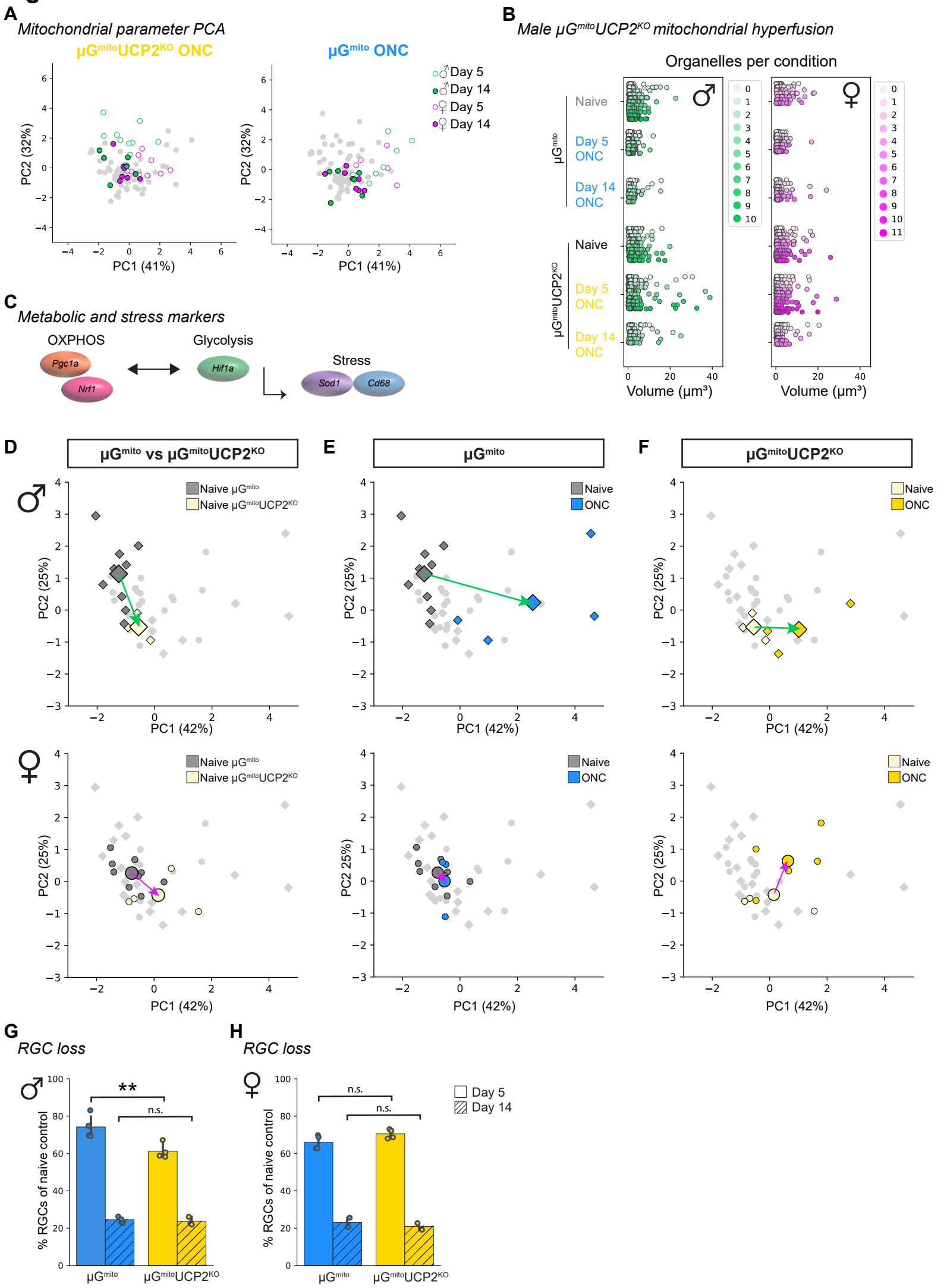
A
Mitochondrial parameter PCA
μGmitoUCP2KO ONC
μGmito ONC
Day 5
Day 14
Day 5
Day 14
PC2 (32%)
PC1 (41%)
B
Male μGmitoUCP2KO mitochondrial hyperfusion
Organelles per condition
μGmito
Naive
Day 5 ONC
Day 14 ONC
μGmitoUCP2KO
Naive
Day 5 ONC
Day 14 ONC
Volume (μm³)
C
Metabolic and stress markers
OXPHOS
Pgc1a
Nrf1
Glycolysis
Hif1a
Stress
Sod1
Cd68
D
μGmito vs μGmitoUCP2KO
Naive μGmito
Naive μGmitoUCP2KO
PC2 (25%)
PC1 (42%)
E
μGmito
Naive
ONC
F
μGmitoUCP2KO
Naive
ONC
G
RGC loss
% RGCs of naive control
**
n.s.
μGmito
μGmitoUCP2KO
H
RGC loss
n.s.
n.s.
Day 5
Day 14

Figure S1

A *Candidate mitochondrial genes enriched in retinal microglia*

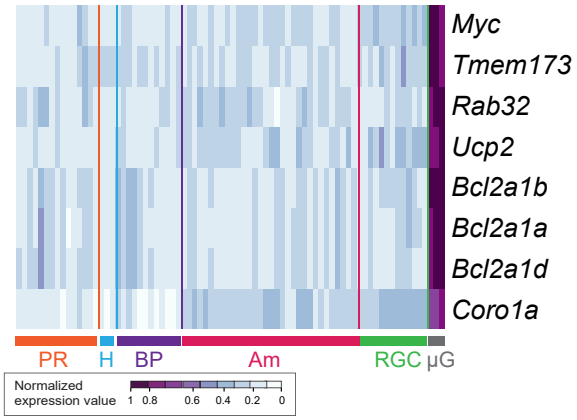

B *Relative Ucp2 expression among retinal cell types*

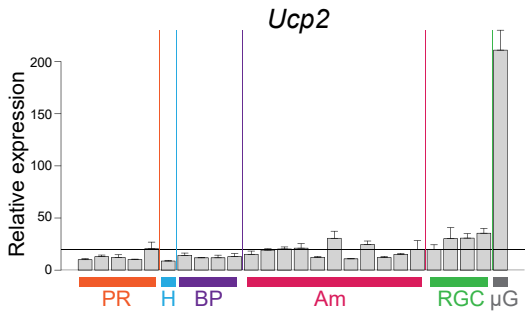

C *Tamoxifen injection timeline*

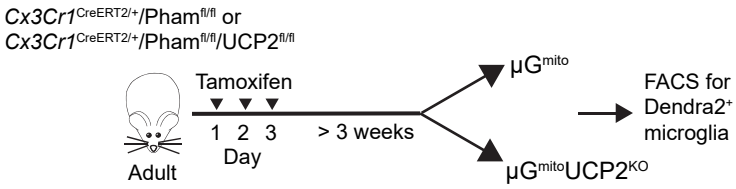

D *Ucp2 transcript level by RT-qPCR*

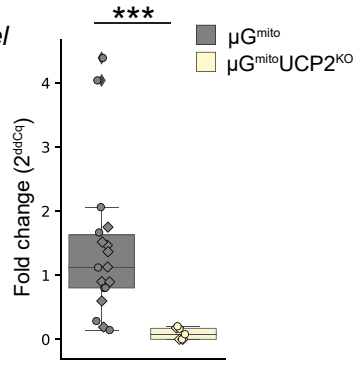

E *Experimental design for primary culture*

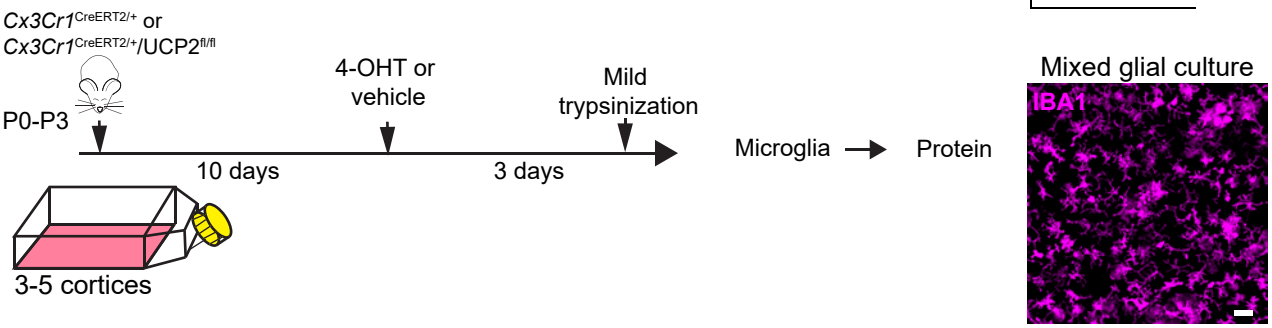

F *Western blot analysis*

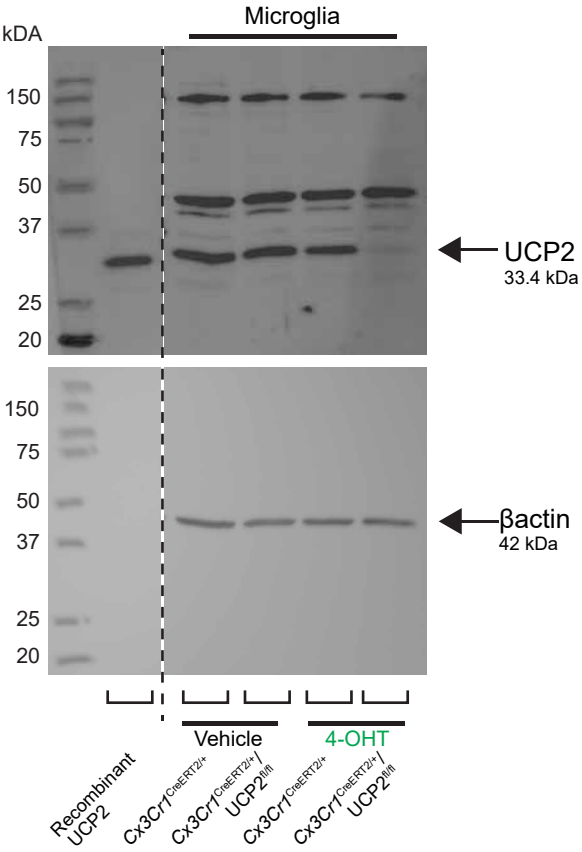

G *Quantification of Western blot bands*

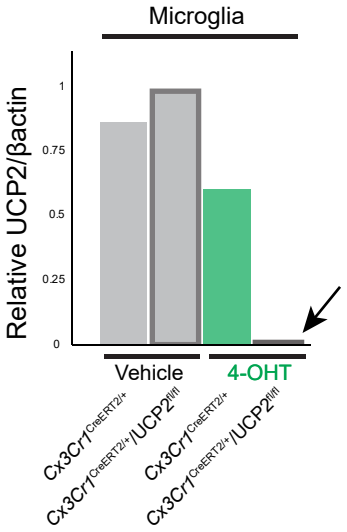

Figure S2

A *Progressive retinal ganglion cell loss after optic nerve crush (ONC)*

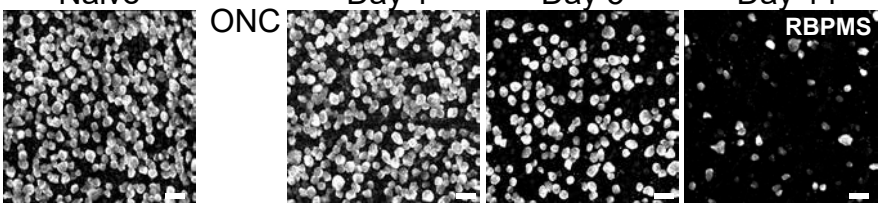

B *IPL microglia after ONC or sham surgery*

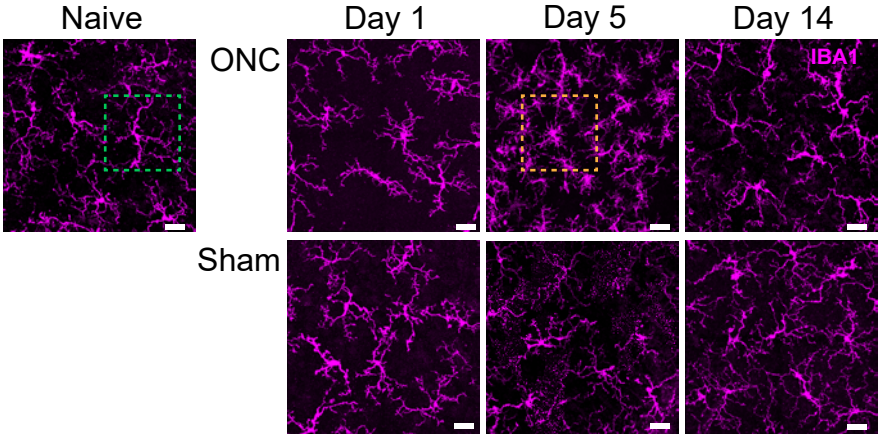

D *Representative CD68 immunostaining*

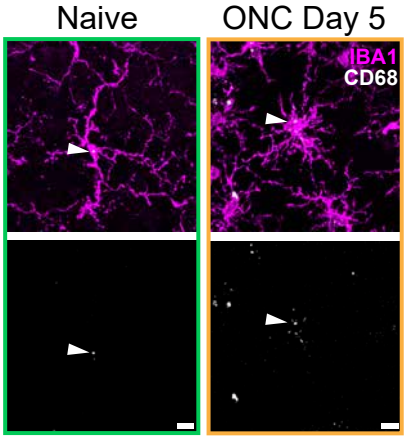

C *IPL microglia Sholl intersections*

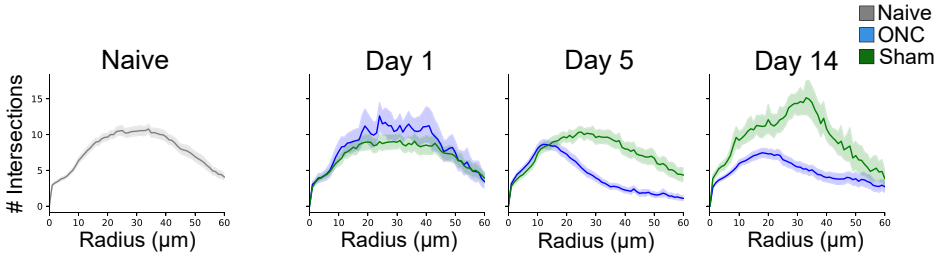

E *CD68 volume in IPL microglia*

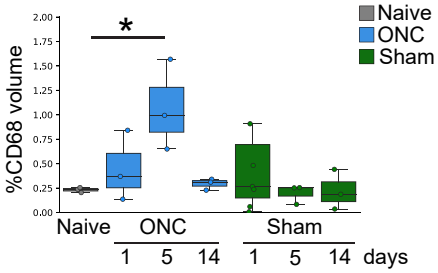

F *OPL microglia after ONC or sham surgery*

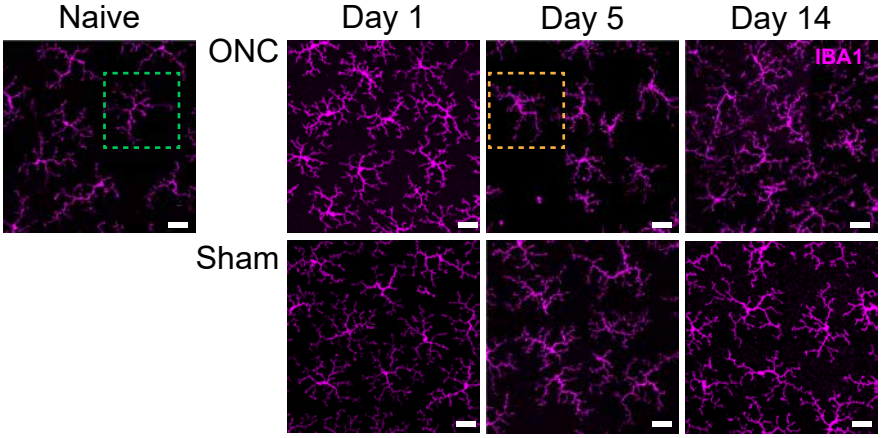

H *Representative CD68 immunostaining*

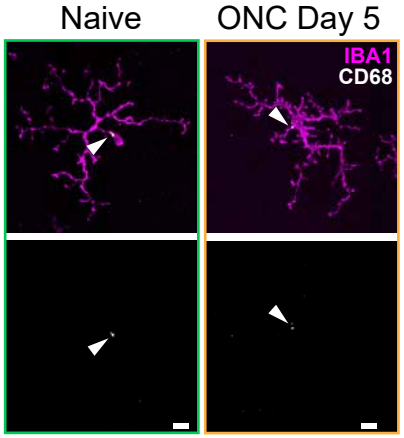

G *OPL microglia Sholl intersections*

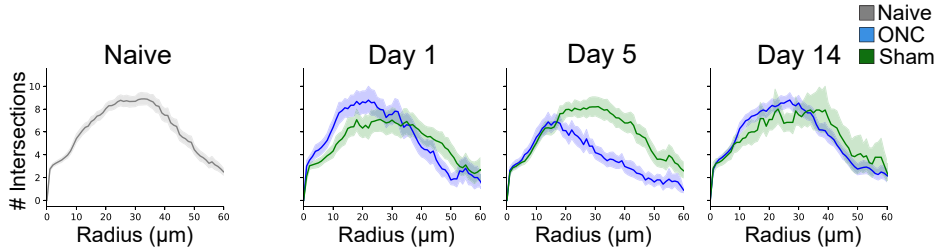

I *CD68 volume in OPL microglia*

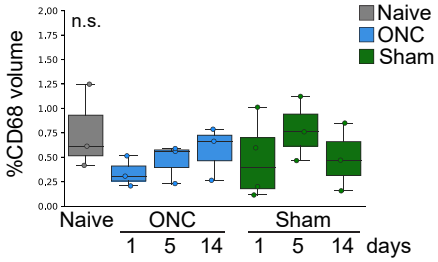

Figure S3

A

PC loadings from seven parameters

	PC 1	PC 2
% Mitochondria volume/microglia	0.220362	0.629862
Median mitochondria volume	-0.34296	0.514091
% CD68 peripheral	0.13551	-0.36167
Number of organells	0.378888	-0.29817
% Mitochondria perinuclear	0.456013	0.255364
Sholl index	0.470127	0.227415
% CD68 volume	0.492882	-0.04842

Sholl index and CD68 parameter PCA

Separated by condition

Conditions separated by sex

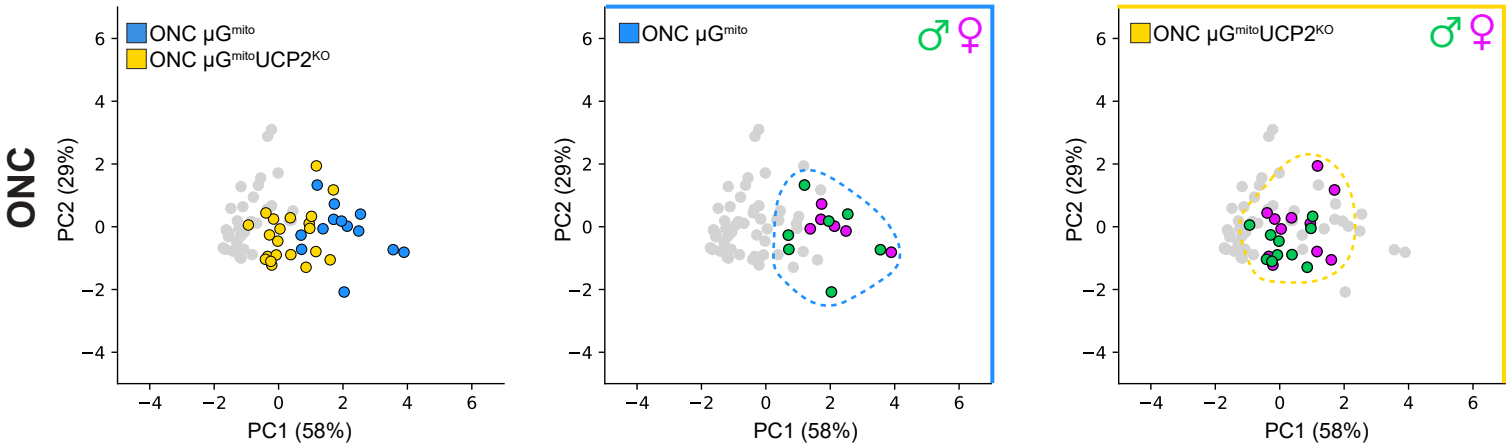

E

PC loadings from mitochondria PCA

	PC 1	PC 2
% Mitochondria volume/microglia	0.123798	0.7945075
Median mitochondrial volume	-0.576187	0.4279728
% Mitochondria perinuclear	0.5185627	0.4166628
Number of organelles	0.6194963	-0.109495

F

Mitochondrial connectivity

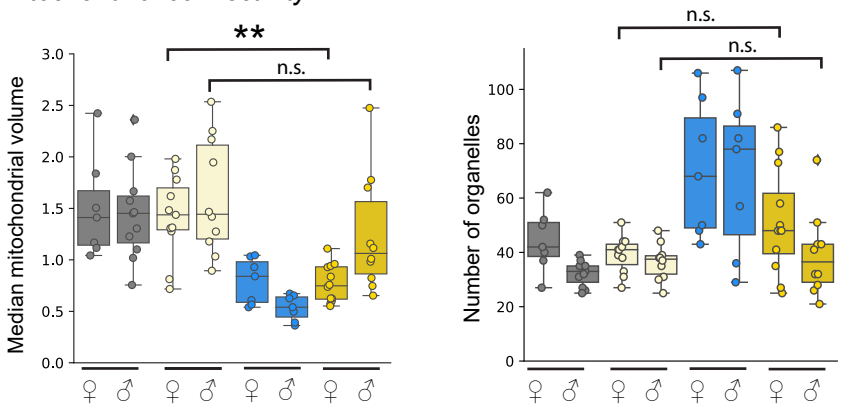

G

Mitochondrial content

H

Mitochondrial localization

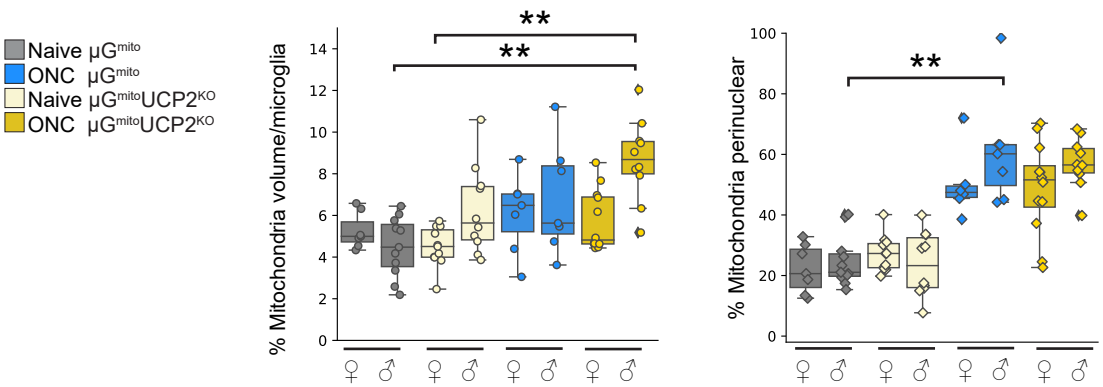

Figure S4

Mitochondrial parameter PCA

A

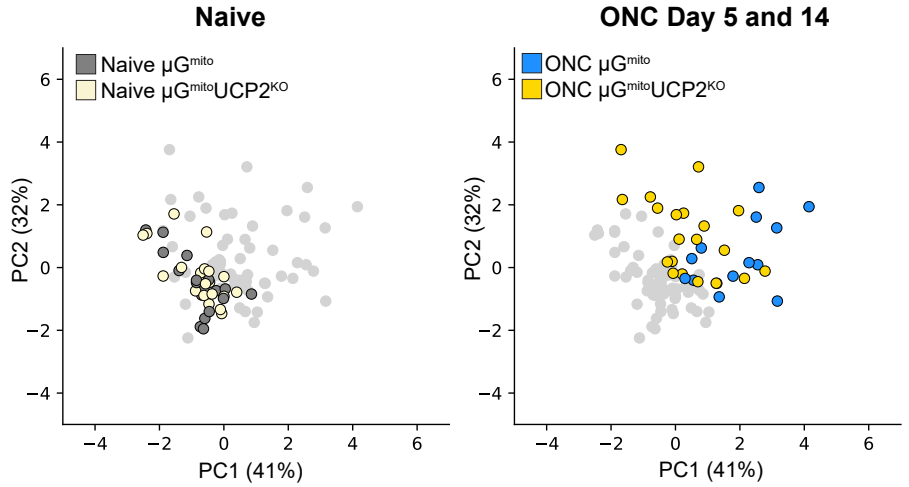

B

PC loadings for metabolic and stress genes

	PC 1	PC 2
Pgc1α	0.60227	0.10366
Nrf1	0.50238	0.06933
Hif1α	0.48479	0.4826
Sod1	-0.2558	0.67006
Cd68	-0.2906	0.55005

C

Naive microglia similar between sexes in μG^mito and μG^mitoUCP2^KO

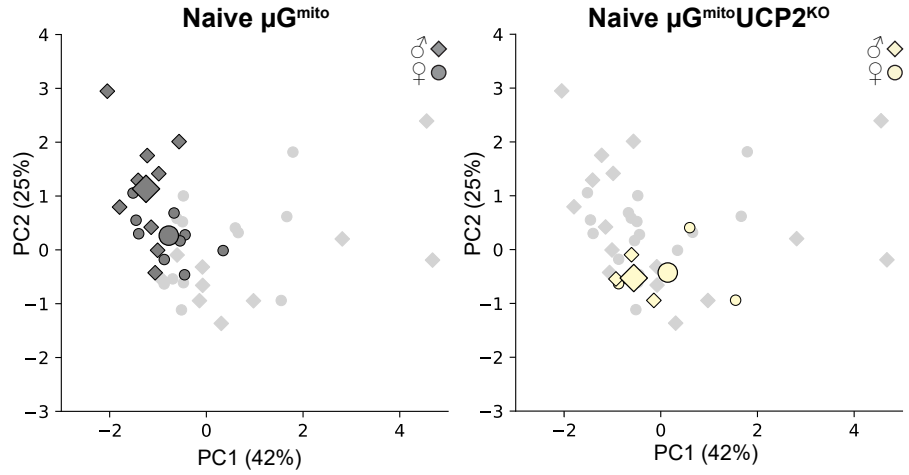

D

Relative expression of male microglia metabolic genes

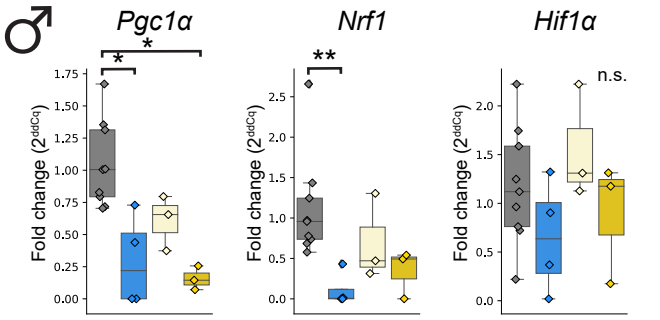

E

Relative expression of female microglia metabolic genes

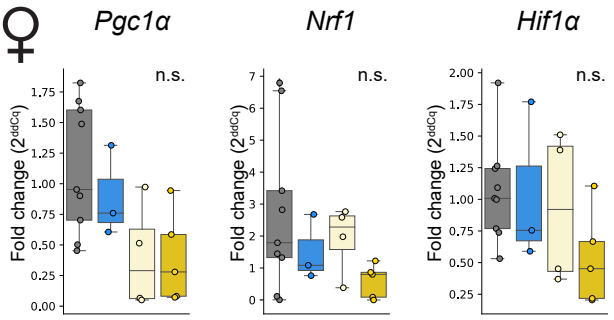

F

Male μG^mitoUCP2^KO ONC microglia greater stress markers

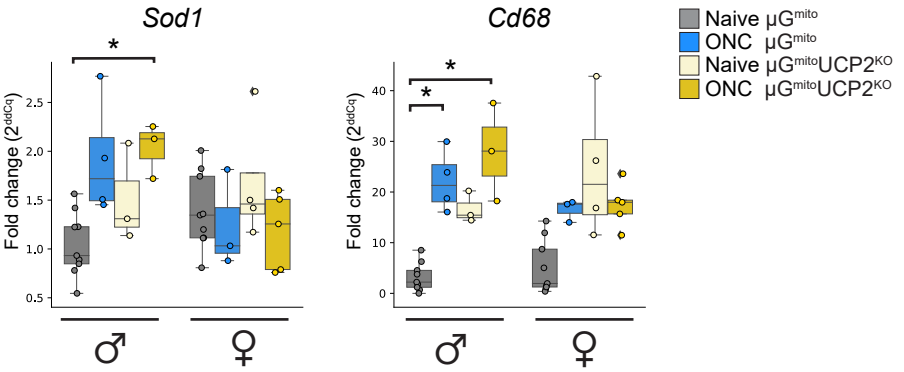

Table S1. Primer sequences.

Gene	Primer	Sequence	Product length
GAPDH	FW	ACAGCAACTCCCACTCTTC	131 bp
	REV	CATTGTCATACCAGGAAATGAGC	
IBA1	FW	ATGAGGATCTGCCGTCCAAAC	114 bp
	REV	CAAGTTTCTCCAGCATTCGCTTC	
GFAP	FW	ATGAGGATCTGCCGTCCAAAC	243 bp
	REV	CAAGTTTCTCCAGCATTCGCTTC	
UCP2	FW	AAGTGTTTCGTCTCCCAGCC	188 bp
	REV	GGGACCTTCAATCGGCAAGA	
PGC1a	FW	CGTGTTCCCGATCACCATATTC	102 bp
	REV	GGTGTCTGTAGTGGCTTGATTC	
NRF1	FW	GGTGAAATAAGCCTCCCGATAG	110 bp
	REV	TGAGGCAGTTTAGACAGAATGG	
CD68	FW	CCTCTGTTCCTTGGGCTATAAG	105 bp
	REV	ATTGAGGAAGGAACTGGTGTAG	
HIF1a	FW	AGGATGAGTTCTGAACGTCGAAAAG	208 bp
	REV	CACTGTCTAGACCACCGGCA	
SOD1	FW	CACTTCGAGCAGAAGGCAAGC	186 bp
	REV	ATGCCTCTCTTCATCCGCCG	

Table S2. Antibody table.

Antibody	Dilution	Source	Catalog No.	RRID
Rabbit anti-IBA1	1:500	GeneTex	GTX100042	AB_1240434
Goat anti-IBA1	IHC: 1:250 WB: 1µg/ml	Abcam	ab 5076	AB_2224402
Rat anti-CD68	1:500	Bio-Rad	MCA1957	AB_322219
Rabbit anti-RBPMS	1:200	Abcam	ab194213	AB_2920590
UCP2	1:1000	Pohl Lab, purified at Pineda	NT-Tier2	n/a
β-actin	1:5000	Sigma	A5441	AB_476744
Goat anti-rabbit IgG (H+L) Alexa Fluor 568	1:2000	ThermoFisher	A11036	AB_10563566
Goat anti- rat IgG (H+L) Alexa Fluor 647	1:2000	ThermoFisher	A21247	AB_141778
Donkey Anti-Guinea Pig IgG (H+L) Alexa Fluor 647	1:1000	Jackson ImmunoResearch	706-605-148	AB_2340476
Donkey anti-rabbit IgG (H+L) Alexa Fluor 568	1:2000	ThermoFisher	A10042	AB_2534017
Donkey anti-goat IgG (H+L)	1:2000	ThermoFisher	A11057	AB_2534104
Donkey anti-goat Alexa Fluor 568 IgG (H+L) Alexa Fluor 488	1:2000	ThermoFisher	A11055	AB_2534102
Donkey anti-rabbit IgG (H+L) Alexa Fluor 488	1:2000	ThermoFisher	A21206	AB_2535792
Donkey anti-Rat IgG (H+L) Antibody DyLight 650	1:2000	ThermoFisher	SA5-10029	AB_2556609
Donkey anti-Rat IgG (H+L) Alexa Fluor 488	1:2000	ThermoFisher	A21208	AB_2535794
Donkey anti-rabbit IgG (H+L) Alexa Fluor 647	1:2000	ThermoFisher	A31573	AB_2536183